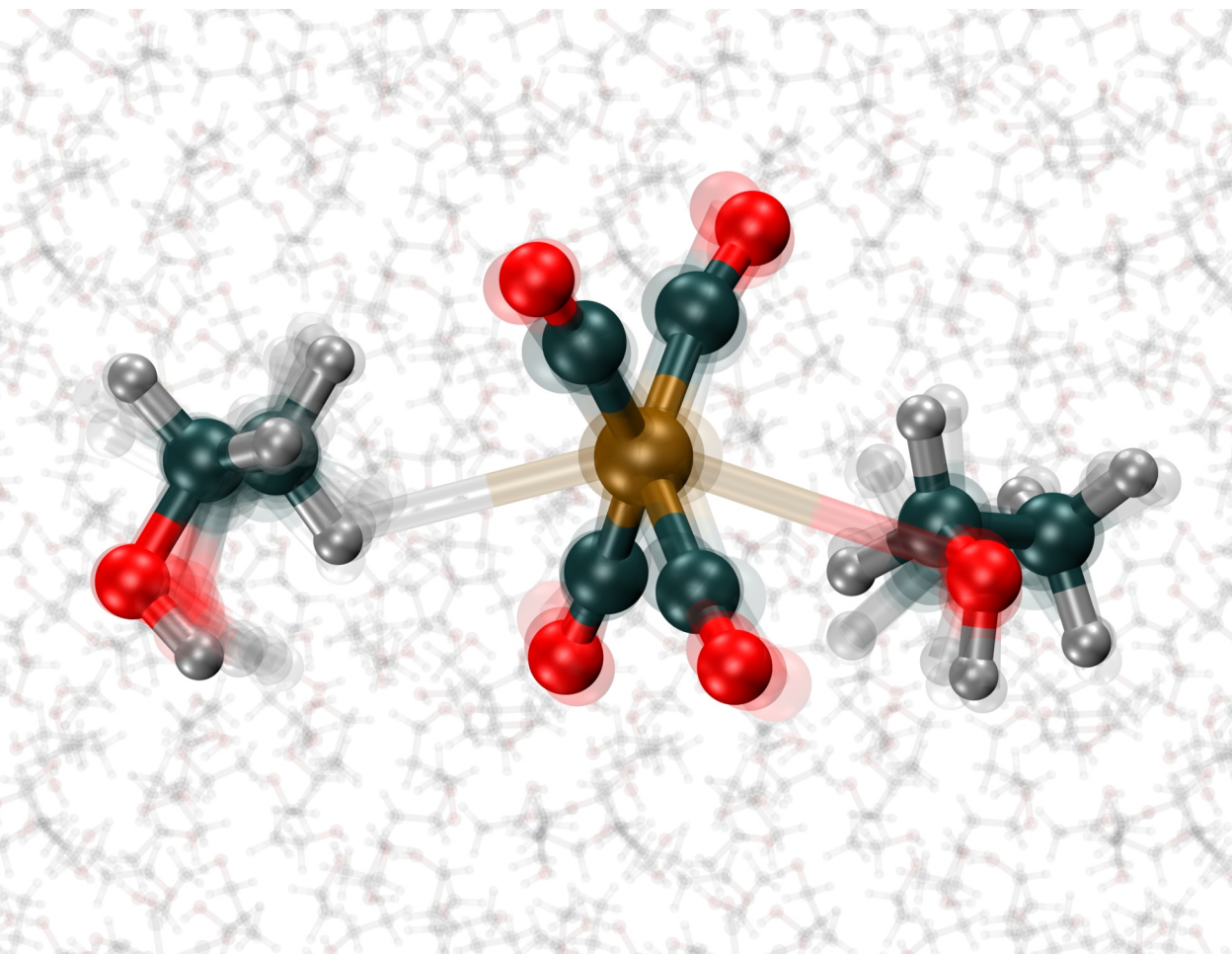


Fundamental interactions in transition metal reactions

Michael R. Coates



Fundamental interactions in transition metal reactions

Michael R. Coates

Academic dissertation for the Degree of Doctor of Philosophy in Chemical Physics at Stockholm University to be publicly defended on Tuesday 26 March 2024 at 13.00 in sal FP41, hus 1, AlbaNova universitetscentrum, Roslagstullsbacken 33.

Abstract

Transition metal complexes that participate in homogeneous reactions often perform the role of a catalyst, facilitating novel reaction pathways. When these complexes are pushed away from their equilibrium, the arrangement of the coordinating ligands around the metal center is perturbed and new reaction pathways are opened. By using a light-induced “trigger” to push the metal complex away from its equilibrium, this process can be initiated with precision. This thesis is concerned with the theoretical understanding of light-induced “triggered” reactions that generate transient, short-lived photoproducts in solution, capable of reacting with the surrounding solvent medium. A combination of theoretical and experimental tools are employed to give precise information about the formation and decay of these transient photoproducts.

In an effort to understand the innate differences between a broad range of transition metal complexes, electron configurations of the metal and its coordinating ligands are a natural starting point. These distinct electronic structures define the physical structure of the transition metal complex and explain the reactivity *or* lack of reactivity of the transition metal complex. To describe these electronic structures, robust quantum chemistry methods are required. Coinciding with these methods is a theoretical framework that aims to simulate the evolution of molecules by means of a molecular dynamics simulation.

The present work involves the study of ironpentacarbonyl or $\text{Fe}(\text{CO})_5$ which we use to explain the reactive landscape of a broad class of carbonyl coordinated transition metal complexes. The part of the thesis devoted to $\text{Fe}(\text{CO})_5$ is divided into distinct sections (i) the short-time (femtosecond-to-picosecond) gas-phase excited state molecular dynamics that produces the transient species, (ii) the long-time (picosecond-to-nanosecond) liquid-phase ground state molecular dynamics which describes the intermediates formed by the transient species and (iii) the experimental probes of the former sections. A final part of the thesis connects carbonyl containing metal complexes to another broad and detailed class of nitrosyl containing metal complexes.

Keywords: *quantum chemistry, electronic structure, multiconfigurational, density functional theory, molecular dynamics, excited state molecular dynamics, non-adiabatic dynamics, solvation, organometallic complexes, x-ray absorption spectroscopy, photoelectron spectroscopy, time-resolved spectroscopy, femtosecond, picosecond.*

Stockholm 2024

<http://urn.kb.se/resolve?urn=urn:nbn:se:su:diva-226430>

ISBN 978-91-8014-671-5
ISBN 978-91-8014-672-2



Stockholm
University

Department of Physics

Stockholm University, 106 91 Stockholm

FUNDAMENTAL INTERACTIONS IN TRANSITION METAL
REACTIONS

Michael R. Coates

Fundamental interactions in transition metal reactions

Michael R. Coates

©Michael R. Coates, Stockholm University 2024

ISBN print 978-91-8014-671-5

ISBN PDF 978-91-8014-672-2

Printed in Sweden by Universitetsservice US-AB, Stockholm 2024

Contents

List of Papers	v
Author's contribution	vii
List of Figures	ix
1 Introduction	15
1.1 Metal carbonyls	17
1.2 This thesis	18
2 Methods	21
2.1 The Molecular Schrödinger Equation	21
2.2 Electronic Structure Theory	24
2.2.1 Wavefunction theory	25
2.2.2 Perturbation theory	28
2.2.3 Density functional theory	29
2.2.4 Coupled cluster theory	32
2.2.5 Summary of electronic structure methods	33
2.3 Nuclear Motion	34
2.3.1 Ground state molecular dynamics	34
2.3.2 Excited state molecular dynamics	37
2.4 Spectroscopy	40
2.4.1 Spectroscopic probes	40
3 Summary of results	47
3.1 Short-time dynamics (< 1 ps)	48
3.1.1 Mechanistic insights into the Fe(CO) ₅ photodissociation process following excitation by 266 nm:	48
3.1.2 Excited state dissociation times of Fe(CO) ₅ and Cr(CO) ₆ following excitation by 266 nm:	53
3.1.3 Probing the excited state lifetimes of Fe(CO) ₅ and Cr(CO) ₆ by photoelectron spectroscopy	56
3.2 Long time dynamics (1 ps - 1 ns)	59

3.2.1	Photoproduct dynamics simulations of $\text{Fe}(\text{CO})_4$ in ethanol solution	59
3.2.2	Probing transient species following photodissociation of $\text{Fe}(\text{CO})_5$ by picosecond L-edge spectroscopy	63
3.2.3	Probing transient species of photodissociated $\text{Cr}(\text{CO})_6$ by picosecond L-edge spectroscopy	67
3.3	From CO to NO	70
3.3.1	Dynamics and electronic structure of an aqueous nitrosyl	70
4	Conclusion and outlook	77
	Populärvetenskaplig sammanfattning	lxxxi
	Acknowledgements	lxxxiii
	References	lxxxv

Abbreviations

AIMD	<i>Ab initio</i> molecular dynamics
BO	Born-Oppenheimer
BOMD	Born-Oppenheimer molecular dynamics
CASSCF	Complete active space self-consistent field
CASPT2	Complete active space second-order perturbation theory
CCSD	Coupled cluster single-double
CI	Configuration interaction
ConIn	Conical intersection
CPCM	Conductor-like polarizable continuum model
CPMD	Car-Parrinello molecular dynamics
DFT	Density functional theory
DLPNO	Domain-based local pair natural orbital
ESMD	Excited state molecular dynamics
FSSH	Fewest switches surface hopping
GGA	Generalized gradient approximation
GSMD	Ground state molecular dynamics
HEXS	Highly excited states
HF	Hartree-Fock
IC	Internal conversion
ISC	Intersystem crossing
KE	Kinetic energy
KS-DFT	Kohn-Sham density functional theory
LDA	Local density approximation
LF	Ligand field

MC	Metal centered
MD	Molecular dynamics
MLCT	Metal-to-ligand charge transfer
MM	Molecular mechanics
MP2	Second-order Møller–Plesset perturbation theory
MRCI	Multi-reference configuration interaction
NEVPT2	Second-order n-electron valence state perturbation theory
PES	Potential energy surface
PNO	Pair natural orbital
PP	Pseudopotential
PW	Plane wave
RASSCF	Restricted active space self-consistent field
RDF	Radial distribution function
RSPT	Rayleigh-Schrödinger perturbation theory
TDDFT	Time-dependent density functional theory
TEY	Total electron yield
TFY	Total fluorescence yield
TRPES	Time-resolved photoelectron spectroscopy
UV-VIS	Ultraviolet-visible
VUV	Vacuum-ultraviolet
WO	Wavefunction overlap
XAS	X-ray absorption spectroscopy
XPS	X-ray photoelectron spectroscopy
XUV	Extreme-ultraviolet

List of Papers

The following papers, referred to in the text by their Roman numerals, are included in this thesis. All published papers are reproduced in this thesis under the CC-BY 4.0 license agreement.

PAPER I: **Photoinduced bond oscillations in ironpentacarbonyl give delayed synchronous bursts of carbonmonoxide release**

Ambar Banerjee, Michael R. Coates, Markus Kowalewski, Hampus Wikmark, Raphael M. Jay, Philippe Wernet, and Michael Odelius,

Nature Communications, **2022**, 13, 1337.

PAPER II: **Varying photo-dissociation mechanisms in $\text{Fe}(\text{CO})_5$ and $\text{Cr}(\text{CO})_6$ from femtosecond valence photoemission and excited-state molecular dynamics simulations**

Henning Schröder,* Michael R. Coates,* Raphael M. Jay, Ambar Banerjee, Nomi Sorgenfrei, Christian Weniger, Rolf Mitzner, Alexander Föhlisch, Michael Odelius and Philippe Wernet,

In preparation.

PAPER III: **Theoretical Investigation of Transient Species following Photodissociation of Ironpentacarbonyl in Ethanol Solution**

Michael R. Coates, Ambar Banerjee, Raphael M. Jay, Philippe Wernet, and Michael Odelius,

In preparation.

PAPER IV: **Photochemical formation and Electronic Structure of an Alkane σ -Complex from Time-Resolved Optical and X-ray Absorption Spectroscopy**

Raphael M. Jay, Michael R. Coates, Ambar Banerjee, Michael Odelius, and Philippe Wernet,

Submitted.

PAPER V: **Spectroscopic Signature of Dynamical Instability of the Aqueous Complex in the Brown-Ring Nitrate Test**

Ambar Banerjee, Michael R. Coates, and Michael Odelius,
Chemistry – A European Journal, **2022**, 28, 54.

PAPER VI: **Simulations of the Aqueous “Brown-Ring” Complex Reveal Fluctuations in Electronic Character**

Michael R. Coates, Ambar Banerjee, and Michael Odelius,
Inorganic Chemistry, **2023**, 62, 41.

The following papers are given Latin characters to distinguish them from the papers that contribute to the thesis directly. When used in the main text, they will be cited as normal references.

PAPER A: **Tracking C–H activation with orbital resolution**

Raphael M. Jay, Ambar Banerjee, Torsten Leitner, Ru-Pan Wang, Jessica Harich, Robert Stefanuik, Hampus Wikmark, Michael R. Coates, Emma V. Beale, Victoria Kabanova, Abdullah Kahraman, Anna Wach, Dmitry Ozerov, Christopher Arrell, Philip J. M. Johnson, Camelia N. Borca, Claudio Cirelli, Camila Bacellar, Christopher Milne, Nils Huse, Grigory Smolentsev, Thomas Huthwelker, Michael Odelius, Philippe Wernet,
Science, **2023**, 380, 6648.

PAPER B: **Accessing Metal-Specific Orbital Interactions in C-H Activation using Resonant Inelastic X-ray Scattering**

Ambar Banerjee, Raphael M. Jay, Torsten Leitner, Ru-Pan Wang, Jessica Harich, Robert Stefanuik, Michael R. Coates, Emma V. Beale, Victoria Kabanova, Abdullah Kahraman, Anna Wach, Dmitry Ozerov, Christopher Arrell, Christopher Milne, Philip J. M. Johnson, Claudio Cirelli, Camila Bacellar, Nils Huse, Michael Odelius, Philippe Wernet,
Chemical Science, **2024**, 15, 2398-2409.

PAPER C: **Ultrafast Mapping of Electronic and Nuclear Structure in the Photo Dissociation of Nitrogen Dioxide**

Zhuang-Yan Zhang, Lorenzo Restaino, Arnab Sen, Marc-Oliver Winghart, Michael R. Coates, Michael Odelius, Markus Kowalewski, Erik T. J. Nibbering, and Arnaud Rouzée,
Submitted.

* denotes that the authors contributed equally.

Author's contribution

Paper I: I analyzed all of the simulation data, wrote all of the analysis code, designed all of the figures and graphical representations of the data and participated in the editing of the manuscript.

Paper II: I analyzed all of the simulation data, wrote all of the analysis code, designed all of the figures and graphical representations of the data and wrote the manuscript (jointly with H. Schröder and P Wernet)

Paper III: I performed all of the quantum chemistry calculations and simulations (jointly with M. Odelius), analyzed all of the simulated data and wrote the manuscript.

Paper IV: I was responsible for the theoretical interpretation of the experimental data, performed all of the calculations, and participated in designing the figures and graphical representations of the data.

Paper V: I analyzed all of the simulation data, wrote all of the analysis code, designed all of the figures and graphical representations of the data and participated in the editing of the manuscript.

Paper VI: I performed all of the quantum chemistry calculations, analyzed all of the simulated data, designed all of the figures and graphical representations of the data and wrote the manuscript.

Text and the overall structure of the methods section were adapted from the licentiate thesis. Fig. 3.2 and Fig. 3.3 from the results section involving $\text{Fe}(\text{CO})_5$ were also re-used. [16]

List of Figures

1.1	A general scheme for a metal which participates in a catalytic cycle. The scheme can be divided into three parts (i) the triggered reaction (ii) the reaction intermediate and (iii) product and recovery of metal catalyst. Adapted from Ref. [70] with permission from the publisher.	16
1.2	A schematic of the possible decay pathways of $\text{Fe}(\text{CO})_5$ in an alcohol solvent.	18
2.1	The description of the complete active space self-consistent field (CASSCF) and restricted active space self-consistent field (RASSCF) method. For CASSCF, all excitations occurring only within the active space are permitted. In RASSCF, the RAS1 subspace allows for at most n -holes allowing for excitations into RAS2 and RAS3. The RAS3 subspace allows for n -electrons. Figure adapted from Ref [59].	27
2.2	(a) A core orbital absorbs an X-ray photon (ω_{in}) which excited it to a unoccupied valence orbital below the continuum. (b) the core-excited state decays via an Auger-Meitner process which results in the filling of the core-orbital and the ejection of an electron from a higher l orbital. (c) the core-excited state decays via the filling of the core-orbital by a valence electron. The result is the emission of a photon of light (ω_{out}).	41
2.3	(a) A pump pulse excites the system to the S_2 excited state. A probe pulse ionizes the neutral molecule by exciting the molecule to the lowest cationic state, D_0 , where the excess energy results in the photoelectron kinetic energy (KE). (b) Following internal conversion (IC), the excited molecule non-radiatively decays to S_1 . The probe interacts with the S_1 state by exciting the molecule to the lowest cationic state, D_0 , which results in a shift of the photoelectron kinetic energy.	44

3.1	The transition metal complexes studied in this thesis (top) along with corresponding solvent molecules studied in relation to each complex (bottom). Top: ironpentacarbonyl ($\text{Fe}(\text{CO})_5$), chromiumhexacarbonyl ($\text{Cr}(\text{CO})_6$) and the “brown-ring” complex ($[\text{Fe}(\text{H}_2\text{O})_5(\text{NO})]^{2+}$). Bottom: ethanol ($\text{C}_2\text{H}_5\text{OH}$), butane (C_4H_{10}) and water (H_2O)	47
3.2	Frontier molecular orbitals of $\text{Fe}(\text{CO})_5$ that give rise to the valence electronic transitions. Transitions formed between the occupied 3d ($3e'$ and $10e''$) orbitals and the unoccupied π_{CO}^* -3d ($4e'^*$) orbitals result in the optically bright MLCT state being populated by a 266 nm pulse. The simplified mechanistic picture of the excited state decay is shown on the right. Adapted from Paper I	49
3.3	Oscillations in the metal-to-ligand charge-transfer (MLCT) state, coloured blue, and the periodic depletion of those states to metal-centered (MC) state of dissociative character, coloured red. Adapted from Paper I	50
3.4	(a-b) The scatter plot of the Fe-C oscillations for all axially dissociating CO ligands. The scatter points indicate the data points originating from the (a) dissociative (red) and (b) bound (blue) states. (c) The average potential energies for all ground and excited states of $\text{Fe}(\text{CO})_5$ at each Fe-C distance for all axially dissociating CO ligands. (d) The fraction of $\text{Fe}(\text{CO})_5$ as a function of time based on the point of no return criteria of 2.5 Å for the axially dissociating CO ligands. A composite figure adapted from data in Paper I and Paper II	51
3.5	Frontier molecular orbitals of $\text{Cr}(\text{CO})_6$ that give rise to the valence electronic transitions.	53
3.6	(a-b) The scatter plot of the Cr-C oscillations for all dissociating CO ligands. The scatter points indicate the data points originating from the (a) dissociative (red) and (b) bound (blue) states. (c) The average potential energies for all ground and excited states of $\text{Cr}(\text{CO})_6$ at each Cr-C distance for all dissociating CO ligands. (d) The fraction of $\text{Cr}(\text{CO})_6$ as a function of time based on the point of no return criteria of 2.6 Å for the dissociating CO ligands. A composite figure adapted from data in Paper II	55

- 3.7 Measured steady-state and time-resolved valence photoelectron spectra of $\text{Fe}(\text{CO})_5$ and $\text{Cr}(\text{CO})_6$ in the gas phase. (a-b) Steady-state spectra of ground-state $\text{Fe}(\text{CO})_5$ and $\text{Cr}(\text{CO})_6$ with assigned metal 3d peaks (photoionization from metal 3d orbitals) and CO π peaks (photoionization from CO π orbitals). (c-d) Time-resolved pump-probe photoelectron intensities of $\text{Fe}(\text{CO})_5$ and $\text{Cr}(\text{CO})_6$ following photoexcitation at 266 nm as a function of pump-probe time delay and up to binding energies of 8 eV just below the metal 3d peaks of ground-state species (intensities encoded in color according to the given color bar, maximum intensities normalized to one by dividing intensities by 1×10^3 for $\text{Fe}(\text{CO})_5$ and by 1×10^4 for $\text{Cr}(\text{CO})_6$, photoelectron intensities at highest binding energies are saturated in this representation). Figure and caption adapted from **Paper II**. 56
- 3.8 Schematic of the main photoionization processes and calculated photoelectron spectra of ground and excited states of $\text{Fe}(\text{CO})_5$ and $\text{Cr}(\text{CO})_6$. Left: Schematic depiction of ground state (GS), excited state (ES, bound and dissociative) and ionized-state potentials as a function of metal (M)-carbon (C) distance. Right: Simplified molecular-orbital energies and electron populations of ground and excited states (bound and dissociative) of $\text{Fe}(\text{CO})_5$ and $\text{Cr}(\text{CO})_6$ (HOMO and one higher-lying orbital, arrows indicate photoionization of the “active electron” in the highest-lying occupied molecular orbital). Figure and caption adapted from **Paper II**. 57
- 3.9 Calculated valence photoelectron spectra of ground states (black), bound excited states (red) and dissociative excited states (blue) of $\text{Fe}(\text{CO})_5$ and $\text{Cr}(\text{CO})_6$ for the indicated metal-carbon distances, plotted up to the 3d peaks of the ground-state species. Figure and caption adapted from **Paper II**. . . . 58

- 3.10 (a) Radial distribution functions $g(r)$ sampled from the $^1\text{Fe}(\text{CO})_5$, $^1\text{Fe}(\text{CO})_4\text{-OH}$ and $^3\text{Fe}(\text{CO})_4$ simulations. The coordination around the iron complexes are seen in $g(r)$ for Fe-H_O , Fe-O_H , Fe-H_C and Fe-C_H . Results for $^1\text{Fe}(\text{CO})_5$ are coloured black, for $^1\text{Fe}(\text{CO})_4\text{-OH}$ are coloured green and for $^3\text{Fe}(\text{CO})_4$ are coloured pink. (b) The distribution of the potential energies from the $^1\text{Fe}(\text{CO})_4\text{-OH}$ and $^3\text{Fe}(\text{CO})_4$ simulations, following the same colour scheme. Both energy distributions are area normalized and the mean of the singlet trajectory is used as reference energy. (c) Representative snapshots from each AIMD simulations, from which two distinct configurations are observed in the $^1\text{Fe}(\text{CO})_4\text{-OH}$ simulation. Figure and caption adapted from **Paper III**. 60
- 3.11 The C-Fe-C axial angles in from the $^1\text{Fe}(\text{CO})_4$ and $^3\text{Fe}(\text{CO})_4$ AIMD simulations. Adapted from Fig. 5(a) in **Paper III** 61
- 3.12 (a) Radial distribution functions $g(r)$ sampled from the $^1\text{Fe}(\text{CO})_4\text{-OH}$ (reproduced from Fig. 3.10), $^1\text{Fe}(\text{CO})_4\text{-HC}_\alpha$ and $^1\text{Fe}(\text{CO})_4\text{-HC}_\beta$ simulations. The coordination around the iron complexes are seen in $g(r)$ for Fe-H_O , Fe-O_H , Fe-H_C and Fe-C_H . The distances from $^1\text{Fe}(\text{CO})_4\text{-OH}$ are coloured green, from $^1\text{Fe}(\text{CO})_4\text{-HC}_\alpha$ are coloured orange and from $^1\text{Fe}(\text{CO})_4\text{-HC}_\beta$ are coloured red. (b) The distribution of the potential energies from the $^1\text{Fe}(\text{CO})_4\text{-OH}$ (reproduced from Fig. 3.10), $^1\text{Fe}(\text{CO})_4\text{-HC}_\alpha$ and $^1\text{Fe}(\text{CO})_4\text{-HC}_\beta$ simulations, following the same colour scheme. All energy distributions are area normalized to account for the differences in simulation length. (c) Representative snapshots from the AIMD simulations for the two distinct minima observed between the Fe-CH coordinated simulations. Figure and caption adapted from **Paper III**. 62
- 3.13 Top: Unpumped Fe 3d L-edge XAS spectrum (denoted “steady-state”) shown in black and the RAS(14,1,2;3,4,7)/TZVP simulated spectrum for $\text{Fe}(\text{CO})_5$ optimized in D_{3h} symmetry. Bottom: The two transient spectra at $t = 0$ ps (orange) and $t = 1000$ ps (blue) following excitation by a 258 nm femtosecond pump pulse. These correspond to the differences between the pumped and unpumped spectra. 63
- 3.14 Top: the RAS(14,1,2;3,4,7)/TZVP simulated spectrum for $^3\text{Fe}(\text{CO})_4$ (green) $^1\text{Fe}(\text{CO})_4\text{-CH}$ EQ (blue) and $^1\text{Fe}(\text{CO})_4\text{-OH}$ AX (red) optimized in C_1 symmetry. Bottom: The transient spectra at $t = 0$ ps (orange). 64

3.15	Top: the RAS(14,1,2;3,4,7)/TZVP simulated spectrum for $^3\text{Fe}(\text{CO})_4$ (green) $^3\text{Fe}(\text{CO})_3\text{-OH}$ (orange) and $^1\text{Fe}(\text{CO})_4\text{-OHAX}$ (red) optimized in C_1 symmetry. Bottom: The transient spectra at $t = 0$ ps (orange) and $t = 1000$ ps (blue).	65
3.16	The photochemical pathways of $\text{Cr}(\text{CO})_6$ following the photoinduced release of CO. Reproduced from Scheme 3 in Paper IV	67
3.17	Steady-state X-ray absorption spectra of $\text{Cr}(\text{CO})_6$ in octane solution measured at the (a) Cr L-edge and (b) O K-edge compared with calculated spectra at the RASSCF and TD-DFT level of theory, respectively. Figure and caption adapted from Fig. 4 in Paper IV	68
3.18	Experimental and calculated transient Cr L-edge X-ray absorption difference spectra of $\text{Cr}(\text{CO})_6$ in octane solution. Figure partially reproduced from Fig. 5 in Paper IV	69
3.19	Snapshots taken from the simulation showing the equilibrium between $[\text{Fe}(\text{H}_2\text{O})_5(\text{NO})]^{2+}$ and $[\text{Fe}(\text{H}_2\text{O})_4(\text{NO})]^{2+}$ through the exchange of one H_2O . (a) shows the octahedral $[\text{Fe}(\text{H}_2\text{O})_5(\text{NO})]^{2+}$ complex. (b) The intermediate state with one equatorial H_2O molecule dissociating from the penta-aqua complex. (c) depicts the formation of the square-pyramidal $[\text{Fe}(\text{H}_2\text{O})_4(\text{NO})]^{2+}$ complex, Figure and caption adapted from Fig. 1 in Paper V	71
3.20	Radial distribution functions, $g(r)$, renormalized at the first peak to enhance features, for the five coordinating water molecules with respect to the Fe center for the Fe- O_w distance. Figure and caption adapted from Fig. 1 in Paper V	72
3.21	Molecular orbital diagram corresponding to the CAS(13e,10o) active space used in the NEVPT2 calculations. The natural orbital occupations corresponding to the SA(1Q+1S)-CAS(13e,10o)/NEVPT2 + CPCM(water) calculation are displayed above in parentheses. Figure and caption reproduced from Paper VI	72
3.22	State properties for a rigid scan along the Fe-N scan calculated for the quartet (blue) and sextet (red) states at the SA(10Q+9S)-CAS(13e,10o)/NEVPT2 level of theory. (a) Potential energy curves of the electronic states. The ground state quartet and sextet states are shown bolded, with all excited states shown more transparent. (b) Weights of leading quartet electron configurations $^4\Psi_1$ (solid blue), $^4\Psi_2$ (dot-dashed blue), $^4\Psi_3$ (dashed blue) and $^4\Psi_5$ (dotted blue) and the leading sextet electron configurations $^6\Psi_1$ (solid red) and $^6\Psi_2$ (dashed red). Figure and caption partially adapted from Paper VI	74

3.23 Difference in NEVPT2 energies (sextet–quartet) for geometries sampled from the quartet and sextet trajectories. The penta-aqua sampled geometries are shown in red and the tetra-aqua sampled geometries are shown in blue. The geometries sampled from the quartet trajectory are shown as solid, while the geometries sampled from the sextet trajectory are shown to be hollow. The difference in energy taken from the model potentials in Figure 5a is shown by the dashed black line. Figure and caption reproduced from **Paper VI**. . . . 75

1. Introduction

Many important chemical reactions take place in the liquid phase. When all of the reactants are in the liquid phase, the reaction is termed *homogeneous*. Homogeneous chemical reactions involving transition metal complexes have been at the forefront of modern chemistry in the latter half of the 20th century.¹ In biology, third-row transition metals participate in several important reactions namely electron transport in mitochondria facilitated by iron-sulfur clusters contained in proteins [36]; cobalt containing corrin complexes in vitamin B₁₂ which act as a coenzyme in enzyme-catalyzed reactions [47]; and the transport of O₂ via an iron porphyrin complex in hemoglobin. [58] With respect to hemoglobin, an open coordination site on the iron center permits the reversible binding of O₂ allowing for oxygen transport into cells. The resulting Fe-O₂ bond can involve several descriptions of the iron center, Fe(II)-O₂ (S=0), Fe(II)-O₂ (S=1) or Fe(III)-O₂⁻ (S=1/2), and involving states of different multiplicity. [58] In the context of organic synthesis, transition metal complexes are most often associated with facilitating novel synthetic pathways through *catalysis*. The addition of these catalysts to an organic reaction is essential in accelerating reaction rates, steering chemical selectivity or allowing for the formation and breaking of bonds that would otherwise be difficult to achieve under normal reaction conditions. Two prominent examples of this are the formation of carbon-carbon (-C=C-) bonds via cross-coupling reactions [43] and the activation and functionalization of inert carbon-hydrogen (-C-H) bonds. [17] In these reactions, the metal center accommodates a change in bonding through processes that involve ligand exchange or reduction/oxidization or both. Certain rhodium-carbonyl complexes (Tp^{*}Rh(CO)₂) in room temperature alkane solvent have shown the ability to activate C-H bonds. [11] Here the fully coordinated complex loses a CO ligand in solution to yield a coordinatively unsaturated² complex that binds an alkane molecule from the surrounding solvent via its C-H bond. This three center, two electron bond forms between the alkane σ -(C-H) orbital and the rhodium metal, followed by a breaking of the bond via ligand rearrangement on the metal center. To facilitate this process, the rhodium in its Rh(I) oxidation state is

¹Nobel Prize in Chemistry 1963, 1973, 2005, 2010, 2022

²We will use the term “undercoordinated” in this thesis.

oxidized to Rh(III) resulting from the structural changes around the metal.

To understand how these reactions proceed so that we can improve the design of better metal catalysts, we need to unambiguously determine the mechanisms which lead to chemical transformations and describe the structures (and electronic structures) involved. Encoded within these reactions are changes in electron configuration, in spin states, in coordination, and in solvation. These are common ingredients in homogeneous catalysis involving transition metal complexes which need to be disentangled. This is, however, not easy since many different changes may occur on overlapping time scales and we do not know when the reaction will begin and at what times the intermediate steps will occur. For this we seek a “trigger” which will initiate the reaction. This trigger provides a precise starting point, synchronizing the reaction and allowing for the repeated measurement.

This thesis concerns itself with so-called triggered reactions. In this context, the reaction trigger is an optical (visible to ultraviolet wavelength) excitation which initiates the chemical reaction. This excitation serves as a starting point for a more general reaction scheme summarized in Scheme. 1.1, which as shown, describes a complete catalytic process involving a generic metal catalyst. In the initial step, the metal catalyst exists in a pure solvent medium or a solution containing an additional reactant molecule. Upon excitation, the metal catalyst is brought away from its equilibrium structure and forms a bond with the surrounding molecule(s) to produce a reaction intermediate. In a final step, the newly coordinating molecule undergoes structural (bond breaking/bond formation) or electronic changes (increase or decrease in total number of electrons) resulting in a new molecule. The remaining metal catalyst returns to its equilibrium structure.

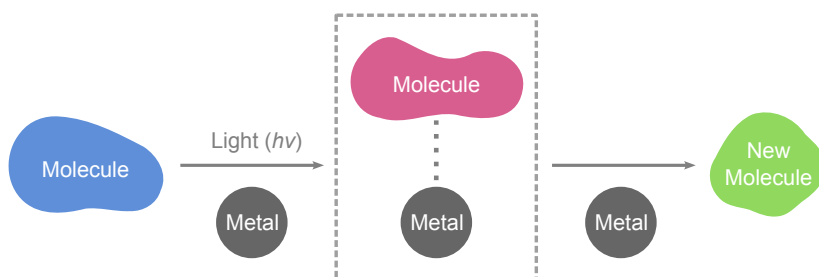


Figure 1.1: A general scheme for a metal which participates in a catalytic cycle. The scheme can be divided into three parts (i) the triggered reaction (ii) the reaction intermediate and (iii) product and recovery of metal catalyst. Adapted from Ref. [70] with permission from the publisher.

The first part of this scheme is considerably different from the rest, where it is concerned with femtosecond (fs) to picosecond (ps) excited state dy-

namics of metal complexes. When these complexes are photoexcited, the excited state population can decay by the nonradiative processes of internal conversion (IC) and intersystem crossings (ISC). These states of the same or different multiplicity form a breakdown of the initial metal complex which results in an intermediate that is undercoordinated, serving as a starting point for a catalytic reaction. We are interested in the mechanistic steps that lead to the breakdown of the initial metal complex since they allow us to understand how these undercoordinated complexes are formed.

The second part of the scheme involves long time (picosecond to nanosecond) dynamics of the undercoordinated complex as it coordinates nearby solvent molecules. This part of the reaction coordinate is dominated by bond formation, re-organization of the molecule and ligands around the metal complex (isomerization). Implicit in the coordination of the metal complex by the solvent is a necessity to describe the metal-solvent degrees of freedom.

1.1 Metal carbonyls

The scheme above presents an illustrative picture of the kinds of processes that we want to study, however, we require a real metal complex. A class of systems catalyzing/participating in these reactions are transition metal complexes with coordinating carbonyl ligands. Metal carbonyls have been studied for their photo-induced reactivity since the 1970s [73] and in the intermediate years, several trends have been identified. [49; 68] A general trend observed in metal carbonyls is that irradiation with UV-visible light results in the sub-picosecond “release” of a CO ligand. The release of CO from metal carbonyls has been observed in nearly all commonly used solvents in organic synthesis, specifically alcohols (-OH), alkanes (-CH), silanes (-SiH) and cyclic hydrocarbons (-CH₂). [49; 56; 68; 73] Following the initial photodissociation, these complexes have been shown to form catalytically reactive intermediates, namely complexes containing rhodium and iridium that activate C-H bonds [7; 11] and M(CO)₆ (M = Cr, Mo, W) reactions in alkenes to facilitate cis-trans isomerization and hydrogenation reactions. [73] At intermediate timescales (fs - ps) some metal carbonyls exhibit strong spin state interactions that facilitate the coordination of a solvent molecule or leave the undercoordinated complex inert. [37; 38] In these systems, the interplay of the spin state dynamics has been debated [14; 23] and discussed [38] as being essential in describing the reactivity of the intermediate complex.

Within this set of metal carbonyls, ironpentacarbonyl or Fe(CO)₅ can be

considered an ideal system because it exemplifies the aforementioned dynamics and reactivity of metal carbonyls. The sub-picosecond dynamics involve the release of CO in a variety of solvents [8; 53; 61; 62] leading to the production of $\text{Fe}(\text{CO})_4$ in the singlet and triplet states. In order to understand the reaction coordinate of $\text{Fe}(\text{CO})_5$, we redefine the scheme in Fig. 1.1 with a system specific overview in Fig. 1.2

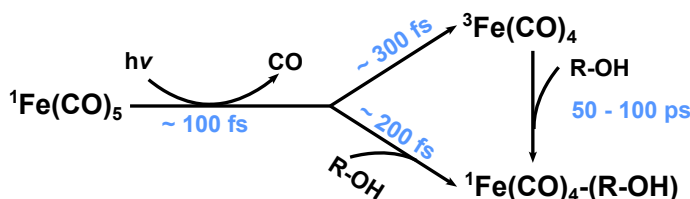


Figure 1.2: A schematic of the possible decay pathways of $\text{Fe}(\text{CO})_5$ in an alcohol solvent.

The dynamics of $\text{Fe}(\text{CO})_5$ are divided into two reaction timescales, short (< 1 ps) and long (1 ps - 1 ns). In both the gas-phase and in room temperature alcohols, the short timescale reactions of $\text{Fe}(\text{CO})_5$ involve a rapid loss of a CO ligand. To date, much of the short time dynamics has been studied exclusively in the gas-phase by a series of studies, [29; 30; 66] yielding time-constants of the dissociation of $\text{Fe}(\text{CO})_5$ into $\text{Fe}(\text{CO})_4$.

The liquid phase dynamics are more complicated, involving rapid coordination of an alcohol solvent within 200 fs in the singlet pathway [34; 71] that competes with the formation of an unreactive triplet state on a similar timescale (300 fs). [38; 62] In the singlet state, free $\text{Fe}(\text{CO})_4$ is a highly reactive undercoordinated complex [51] that reacts with an available or “token” solvent molecule that exists nearby. [38] It has been proposed by Besora et al. [8] that while the triplet state is unreactive, it possibly forms a weak interaction that leads to ISC to form the singlet $\text{Fe}(\text{CO})_4$ on the timescale of 50-100 ps.

1.2 This thesis

The structural and electronic changes highlighted above can be considered fundamental ingredients in transition metal catalysis. The aim of this thesis is to provide a theoretical understanding of these fundamental ingredients through quantum chemical calculations and molecular dynamics simulations. We use the photochemistry of $\text{Fe}(\text{CO})_5$ as a template to discuss the topics and we divide this thesis into the following parts:

- The short time (< 1 ps) dynamics of $\text{Fe}(\text{CO})_5$ are summarized from

Paper I where we simulate gas-phase femtosecond excited state dynamics. We relate the results of this study directly to another well-studied complex chromiumhexacarbonyl or $\text{Cr}(\text{CO})_6$ in an effort to learn the mechanistic pathways that lead to varying dissociation dynamics. These results are summarized in **Paper II**, where we make an explicit comparison of both systems to the results of a time-resolved spectroscopy experiment. These studies aim to characterize the initial photoproduct dynamics that yield undercoordinated metal complexes.

- The long time (1 ps - 1 ns) dynamics of $\text{Fe}(\text{CO})_4$ are simulated in bulk ethanol liquid in the singlet and triplet states to contrast and understand the spin state interactions and solvent dynamics (**Paper III**). We relate the structural information from the simulations to the results of a time-resolved X-ray study of $\text{Fe}(\text{CO})_5$ in ethanol. In this section we also present the results a time-resolved X-ray study of $\text{Cr}(\text{CO})_6$ in octane (**Paper IV**). These studies aim to characterize the undercoordinated metal complexes that react in solution.
- In a final section, we connect the carbonyl ligand to the nitrosyl ligand. We summarize **Paper V and VI** where we present the liquid dynamics of the simplest aqueous nitrosyl.

2. Methods

2.1 The Molecular Schrödinger Equation

A complete quantum mechanical description of all molecular interactions is given by the non-relativistic Schrödinger equation, here shown in the time-independent formulation:

$$\hat{H}\Psi = E\Psi \quad (2.1)$$

The molecular Hamiltonian denoted \hat{H} operates on the wavefunction $\Psi(r, R)$ that depends on the spatial positions of both the electrons and nuclei denoted by \mathbf{r}_i and \mathbf{R}_A , respectively. Here the Hamiltonian is expressed in atomic units where the mass of the electron m_e , reduced Planck's constant \hbar , Bohr radius a_0 and electron charge e are four independent units implicitly set to unity. The molecular Hamiltonian describing the kinetic and potential energies of the electrons and nuclei is given by:

$$\hat{H} = \hat{T}_e + \hat{T}_N + \hat{V}_{ee} + \hat{V}_{eN} + \hat{V}_{NN} \quad (2.2)$$

$$\begin{aligned} \hat{T}_e &= -\sum_i \frac{1}{2} \nabla_i^2; \hat{T}_N = -\sum_A \frac{1}{2M_A} \nabla_A^2; \hat{V}_{ee} = \sum_{i < j} \frac{1}{|\mathbf{r}_i - \mathbf{r}_j|} \\ \hat{V}_{eN} &= -\sum_{A,i} \frac{Z_A}{|\mathbf{r}_i - \mathbf{R}_A|}; \hat{V}_{NN} = \sum_{A < B} \frac{Z_A Z_B}{|\mathbf{R}_A - \mathbf{R}_B|} \end{aligned} \quad (2.3)$$

Eq. 2.3 provides two kinetic energy and three potential energy terms describing the kinetic energy of the electrons \hat{T}_e , the kinetic energy of the nuclei \hat{T}_N , the Coulombic interactions via the electron-electron repulsion \hat{V}_{ee} , electron-nuclear attraction \hat{V}_{eN} and nuclear-nuclear repulsion \hat{V}_{NN} . In the expression of the electronic and nuclear kinetic energies, the Laplacian (∇^2) is used to denote the second order partial derivatives of the cartesian coordinates, while i and j are used to denote the i^{th} and j^{th} electrons

and A and B are used to denote the A^{th} and B^{th} nuclei. The solutions to the total wavefunction are effectively impossible. To facilitate the solution of Eq. 2.1, an ansatz with a separation of variables into electronic and nuclear components is done by considering the Born-Oppenheimer expansion:

$$\Psi(\mathbf{r}, \mathbf{R}) = \sum_i \psi_i(\mathbf{r}; \mathbf{R}) \chi_i(\mathbf{R}) \quad (2.4)$$

The separations of the degrees-of-freedom results in the electronic wavefunction ψ_i having a dependence on electronic coordinates and a parametric dependence on nuclear coordinates. Hence the electronic energies can be solved for a particular nuclear configuration. The motivation for this ansatz is that the electronic motion is orders of magnitude faster than nuclear motion due to the mass difference of nuclei and electrons. The solution of the electronic wavefunctions requires a truncated Hamiltonian that operates on electronic degrees-of-freedom. The exclusion of the nuclear kinetic energy (\hat{T}_N) from the molecular Hamiltonian in Eq. 2.2 results in the electronic Hamiltonian:

$$\hat{H}_e = \hat{T}_e + \hat{V}_{ee} + \hat{V}_{eN} + \hat{V}_{NN} \quad (2.5)$$

It follows that the total energy of \hat{H}_e for a particular electronic state (i) is given by:

$$\hat{H}_e \psi_i(\mathbf{r}; \mathbf{R}) = E_i(\mathbf{R}) \psi_i(\mathbf{r}; \mathbf{R}) \quad (2.6)$$

The electronic energies are stationary solutions to Eq. 2.6 that are obtained for each nuclear position resulting in a potential energy surface (PES). Since the electronic and nuclear degrees-of-freedom are decoupled, this picture is sufficient for electronic PESs that are well separated and do not cross. These surfaces are termed *adiabatic*, where the couplings (described in Eqs. 2.8-2.10 below) between surfaces are negligible and hence, neglected. However, it is common for surfaces to cross or have near crossings. In the former case, if the states that cross have different symmetries, then their wavefunctions are unaffected by the degeneracy. If the states have the same symmetry, then they may form *so-called* avoided crossings, where the wavefunctions mix and prevent a degeneracy. Following passage through the avoided crossing, the character of the state described by each wavefunction is changed. In addition to avoided crossings, two electronic states of the same symmetry may form points of degeneracy referred to as *conical intersections* (ConInts). [24] In the vicinity of these crossings, the couplings

between surfaces become non-negligible, where a dynamical description of the electronic and nuclear motion is needed. Thus, the full molecular Hamiltonian including the nuclear kinetic energy operator \hat{T}_N must be used to evaluate the separated wavefunction in Eq. 2.4. Insertion of the wavefunction in Eq. 2.4 into the time-independent Schrödinger equation in Eq. 2.1, left-multiplication by $\psi_j(\mathbf{r}, \mathbf{R})^*$ and integration over electronic coordinates to yield:

$$[\hat{T}_N + E_j(\mathbf{R})]\chi_j(\mathbf{R}) - \sum_i \Lambda_{ji} \chi_i(\mathbf{R}) = E \chi_j(\mathbf{R}) \quad (2.7)$$

The adiabatic potential energy surfaces (E_j) and the nuclear kinetic energy operator are accounted for, and the latter also gives a contribution describing the coupling between the electron and nuclear motion. These non-adiabatic couplings (Λ_{ji}) [74] consist of two different components, a vector (often called derivative coupling (F_{ji})) and a scalar (G_{ji}) contribution formulated as follows:

$$\Lambda_{ji} = \frac{1}{2M} [2F_{ji} \cdot \nabla + G_{ji}] \quad (2.8)$$

$$F_{ji} = \langle \psi_j | \nabla \psi_i \rangle = \frac{\langle \psi_j | \nabla \hat{H}_e | \psi_i \rangle}{E_i - E_j} \quad (2.9)$$

$$G_{ji} = \langle \psi_j | \nabla^2 \psi_i \rangle \quad (2.10)$$

The major contribution to Λ_{ji} , the derivative coupling term, F_{ji} connects nuclear motion on different electronic surfaces and has an inverse dependence on the difference energy between the two surfaces. In many cases the difference in energy between the potential energy surfaces E_j is large and hence the couplings are neglected, however, near avoided crossings the couplings become large as the energy gap tends to zero, while at points of degeneracy at the ConIn, the couplings are infinite. The minor contribution to Λ_{ji} , the scalar coupling term, G_{ji} effects both the interstate coupling ($i \neq j$) and provides a correction to the individual state energies ($i = j$). The G_{ji} are small relative to the F_{ji} and because of the $\frac{1}{2M}$ factor, the G_{ji} are typically neglected [15].

The first part of this section will present a survey of the electronic structure methods used in this thesis. The second part of this section will provide a description of the ground- and excited-state molecular dynamics tools which employ some of the electronic structure methods. The last part of this section will describe the spectroscopic probes that have been used in this thesis.

2.2 Electronic Structure Theory

A natural starting point for the discussion of electronic structure theory is with Hartree-Fock (HF). HF takes the electronic wavefunction in Eq. 2.6 to be a single Slater determinant composed of 1-electron spin-orbitals ($\phi_i(\mathbf{r}) = \psi_i(\mathbf{r}) \omega$) containing both a spatial ($\psi_i(\mathbf{r})$) and spin function *i.e.* $\omega = \alpha$ for “up-spin” or $\omega = \beta$ for “down-spin”. Since electrons are fermions with an intrinsic spin, the Slater determinant is chosen such that the trial wavefunction obeys the Pauli exclusion principle, whereby the exchange of any two electrons results in the change of sign of the wavefunction.

In practice, the HF molecular orbitals are often expanded in terms of atom centered basis functions ($\chi_\nu(\mathbf{r})$):

$$\phi_i(\mathbf{r}) = \sum_{\nu}^{N_{basis}} c_{i\nu} \chi_{\nu}(\mathbf{r}), \quad (2.11)$$

where the coefficients ($c_{i\nu}$) multiply the atom centered basis functions. With a wavefunction ansatz taken to be a single Slater determinant, the wavefunction (and thereby orbital coefficients) is optimized variationally with respect to the E_0 . This corresponds to finding the lowest eigenvalue of Eq. 2.6 to yield a total energy that is an upper bound to the *exact energy* (\mathcal{E}_0) for a chosen 1-electron basis. However the minimization of the E_0 is reformulated into a pseudo-eigenvalue equation of the Fock-operator (\hat{F}), which has the orbital energies as eigenvalues. The difference between the exact energy and the energy from the HF wavefunction is termed *correlation energy* (E_{corr}) and defined as: [39]

$$E_{\text{corr}} = \mathcal{E}_0 - E_{\text{HF}}. \quad (2.12)$$

The source of the correlation energy is in approximations made in the form of the HF wavefunction. The HF implies that each electron is only experiencing an average potential energy of all other electrons, often termed a *mean field approximation*. This assumption is approximate since electrons interact with each other through instantaneous electrostatic interactions (*i.e.* by $1/r_{ij}$). The HF wavefunction is taken to be a single Slater determinant which is often sufficient to describe molecules near their equilibrium structures. However, as bonds become stretched to the point of dissociation, additional electron configurations are needed to correctly describe the electronic wavefunction of the system made up from the fragments.

2.2.1 Wavefunction theory

The use of a single Slater determinant has been discussed above as a source of correlation energy, particularly in the context of forming and breaking bonds where more electron configurations are needed. By taking the 1-electron spin orbitals obtained from the HF wavefunction *i.e.* a single Slater determinant, the wavefunction can be expressed in terms of more electron configurations. This is accomplished by taking the optimized HF wavefunction as a reference wavefunction (Φ_0) and including all possible excited determinants formed within the basis spanned by the 1-electron spin orbitals. The linear combination of excited determinants is referred to as *configuration interaction* (CI) [22]

$$|\psi\rangle = c_0|\Phi_0\rangle + \sum_{r,a} c_a^r |\Phi_a^r\rangle + \sum_{\substack{a<b \\ r<s}} c_{ab}^{rs} |\Phi_{ab}^{rs}\rangle + \sum_{\substack{a<b<c \\ r<s<t}} c_{abc}^{rst} |\Phi_{abc}^{rst}\rangle + \dots \quad (2.13)$$

The first term in the sum corresponds to the reference determinant Φ_0 (the optimized HF wavefunction) and an associated expansion coefficient c_0 . Singly excited determinants and coefficients are denoted Φ_a^r and c_a^r , respectively. Here the Φ_a^r denotes a excited determinant with an excitation from an occupied 1-electron orbital ϕ_a to an unoccupied orbital ϕ_r . This notation is extended to doubly, triply \dots N -tuply excited determinants. For each excitation order, the summation indices *e.g.* $a < b$ and $r < s$, ensure that only unique determinants are considered in the sum.

The wavefunction expansion in the limit of all N -tuple excitations, as shown in Eq. 2.13, is referred to as the “full CI” wavefunction. For an a complete basis set, which would require an infinite number of basis functions, the full CI wavefunction would require an infinite number of excitations. For the occupied and unoccupied orbitals that are complete the 1-electron basis set, the solution of the electronic Schrödinger results in the *exact energy*.

With the exception of a few molecules containing few electrons or a small 1-electron basis, the full CI energy is unattainable. The linear combination of determinants constructing the wavefunction expansion is often truncated to lower order excitations of singly, CI singles (CIS) or singly and doubly, CI singles-doubles (CISD). For bound molecules in near their equilibrium geometry, the ground state description is improved by incorporating the doubles contribution to the wave function.

Much of this thesis involves the study of molecular fragmentation *i.e* bond breaking, which the truncation schemes such as CISD are insufficient in

describing for reasons related to size consistency ($E_{AB} \neq E_A + E_B$, the energies of fragments *A* and *B*). [52] We overcome this particular limitation of the truncated CI wavefunction by considering a subset of chemically meaningful and energetically relevant molecular orbitals. Within this orbital subspace all possible excited determinants are included, without truncating the excitation order. This “multiconfigurational” treatment of the wavefunction is generalized by the *multiconfigurational self-consistent field* (MCSCF) method. [69] In MCSCF, these coefficients of the 1-electron atomic orbital basis functions, $c_{i\nu}$, and the determinant expansion coefficients in Eq. 2.13 are simultaneously optimized. This offers an improvement to the ground state energy but also results in the re-optimization of the orbital coefficients and generates a new set of molecular orbitals.

In practice, the selection of the molecular orbital subspace (denoted an active space) is arbitrary. While there are methods which can identify orbital subspaces based on the density matrix [33] the straightforward selection of an orbital subspace relies on a general chemical intuition. In many organic molecules and transition metal complexes, the chemical bonding includes bonding σ and π orbitals and the anti-bonding σ^* and π^* pairs of orbitals. To describe bond-breaking, the σ/σ^* pairs are most important, however, these are often energetically lower/higher than the highest occupied/lowest unoccupied molecular orbitals and it is customary to include any energetically relevant pairs of π/π^* orbitals. For the calculation of excited states, this is not generally applicable. Instead the occupied and unoccupied orbitals are selected such that excitations between these orbitals can form the excited states of interest.

A common approach to MCSCF is the *complete active space self-consistent field* (CASSCF) [60] method which partitions the occupied and unoccupied orbitals into subspaces shown as shown in Fig. 2.1.

In Fig. 2.1(a), the CASSCF wavefunction is partitioned into a *frozen*, *inactive*, *active* and *secondary* subspace. The *frozen* subspace often contains core-orbitals from all atoms in the molecule which do not participate in bonding and are not re-optimized. The *active* subspace is selected as described above, where a subset of chemically meaningful and energetically relevant molecular orbitals are chosen. The *inactive* subspace contains the remaining occupied molecular orbitals that are included in the optimization procedure but which are left to be fully occupied. Similarly, the *secondary* subspace contains all of the remaining unoccupied orbitals which are determined to not improve the description of the existing active space.

In a final extension on the method, the active space can be additionally partitioned to yield the *restricted active space self-consistent field* (RASSCF)

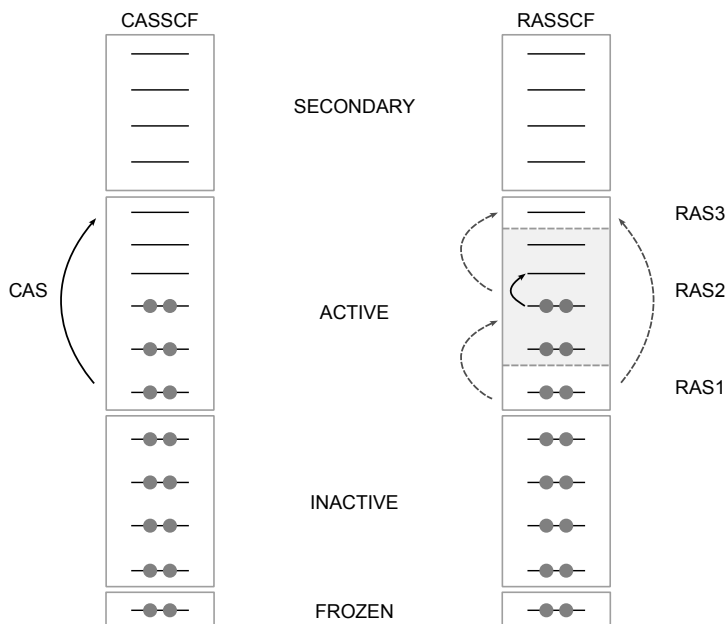


Figure 2.1: The description of the complete active space self-consistent field (CASSCF) and restricted active space self-consistent field (RASSCF) method. For CASSCF, all excitations occurring only within the active space are permitted. In RASSCF, the RAS1 subspace allows for at most n -holes allowing for excitations into RAS2 and RAS3. The RAS3 subspace allows for n -electrons. Figure adapted from Ref [59].

wavefunction shown in In Fig. 2.1(b). We can view RASSCF as a restriction to CASSCF, such that we are able to pick the most important excitations in an otherwise too large CASSCF wavefunction. The *active space* in Fig. 2.1(a) is further partitioned into RAS1, RAS2 and RAS3, where RAS1 is allowed to have at most n -holes allowing for excitations into RAS2 and RAS3, while RAS3 is allowed to have at most n -electrons allowing for the excitations from RAS1 and RAS2. RAS2 allows for all possible excitations within the active space. This partitioning is used in order to calculate core-level spectra, where the core orbitals are placed in the RAS1 subspace and the option to further partition the valence orbital subspaces into RAS2 and RAS3. This method is employed in Openmolcas, where the *highly excited states* (HEXS) restriction is used to allow us to reach the core-level excitations without having to calculate all of the valence excitations.

2.2.2 Perturbation theory

The CASSCF wavefunction offers a significant improvement over HF with respect to the accurate description of bond breaking and fragmentation. Despite this, the overall description of E_{corr} lacks the inclusion of an instantaneous electron-electron interaction. To correct for these interactions, the optimized CASSCF wavefunction is often used as a reference wavefunction in a truncated CI expansion termed a multireference configuration interaction (*e.g.* MRCISD) or as a reference wavefunction in a perturbative approach called CASPT2. [3; 4] In the latter, the CASSCF wavefunction is used in a Rayleigh-Schrödinger perturbation theory (RSPT) much like the HF reference is used in Møller-Plesset perturbation theory to second order (MP2). In CASPT2, the Hamiltonian is partitioned into a zeroth-order Hamiltonian (H_0) plus a perturbation V :

$$H = H_0 + \lambda V \quad (2.14)$$

In MP2, the zeroth-order Hamiltonian is taken to be a one-electron Fock operator (\hat{F}), operating on the HF orbitals which are eigenfunctions of \hat{F} , the Fock operator. In CASSCF, there is an inherent multiconfigurational wavefunction which contains a partially open-shell character, even for a closed shell system. The orbitals obtained from the CASSCF calculation are no longer the same as those obtained in HF and the matrix being diagonalized by \hat{F} no longer has molecular orbital energies as eigenvalues, since the orbitals are different and since there are many determinants in CASSCF. In CASPT2 the description of the zeroth-order Hamiltonian contains on-diagonal terms related to the reference wavefunction and off-diagonal terms that need to be included:

$$\hat{H} = |\Psi^{(0)}\rangle\langle\Psi^{(0)}| \hat{F} |\Psi^{(0)}\rangle\langle\Psi^{(0)}| + \sum_{i,j} |\Psi_i\rangle\langle\Psi_i| \hat{F} |\Psi_j\rangle\langle\Psi_j| \quad (2.15)$$

where $\Psi^{(0)}$ is the CASSCF reference wavefunction and the Ψ_i and Ψ_j correspond to configurations produced by excitations from, for example RAS2 to the *secondary* subspace or to RAS2 from the *inactive* subspace. A common problem with CASPT2 is the presence of “intruder states” which arise due to orbitals which are nearly degenerate to those within the active space. This gives an eigenvalue of \hat{H}_0 which is degenerate with the reference state energy E_0 *i.e.* the CASSCF energy. The solution to the intruder state problem within CASPT2 has been to apply a level shift to increase the orbital energy gap between the inactive and active space orbitals. This arbitrary shift has been shown to effect the state energies of the ground and excited states

of organic chromophores [75] and lacks a universality for the type of system being studied. To remedy this, an alternative definition of the zeroth-order Hamiltonian by Dyall [25] results in the second-order N-electron valence state perturbation theory (NEVPT2) method which does not require a level shift, at the cost of accuracy when compared to CASPT2. We use NEVPT2 extensively in **Paper V** and **Paper VI**.

2.2.3 Density functional theory

The CASPT2, NEVPT2 (and MRCISD) methods are accurate and versatile methods in quantum chemistry, but are computationally very demanding. Hence, alternative formulations are desirable. In a different formulation of electronic structure theory, the electronic density $\rho(r)$ is used as a variable which reduces the degrees-of-freedom from a $3N$ dimensional problem to a 3-dimensional problem of cartesian components. Here the electron density is defined as:

$$\rho(r) = N \int \cdots \int \psi(r_1, r_2, \cdots, r_N)^* \psi(r_1, r_2, \cdots, r_N) dr_2 \cdots dr_N. \quad (2.16)$$

Hohenberg and Kohn showed that the ground state density uniquely defines the ground state energy. [31] Using this ground state density to determine the ground state energy of a system is the domain of density functional theory (DFT). In DFT the total energy is represented in terms of the density function $\rho(r)$ and hence the term “density functional”. The total energy expressed in terms of the density is as follows:

$$E[\rho(r)] = T[\rho(r)] + U[\rho(r)] + V[\rho(r)], \quad (2.17)$$

where $T[\rho(r)]$ is the kinetic energy of the electrons, $U[\rho(r)]$ is the electron-electron interaction energy and $V[\rho(r)]$ is the energy of the electrons interacting with the external potential (from nuclei). The first two terms can be grouped together to form the “universal functional” which is the same for a specific number of electrons while the latter term is system specific and depends explicitly on the position of the nuclei. A central problem of DFT is that this universal functional is shown to exist but we do not know the functional form, therefore approximations are necessary. One approach is given by Kohn-Sham DFT (KS-DFT) which re-introduces molecular orbitals in order to better approximate the kinetic energy functional. The density in Eq. 2.16 (in Slater determinant form) of Kohn-Sham spin-orbitals is expressed as the squares of the orbitals $\rho = \sum_i |\phi_i|^2$. The non-interacting

case allows for the explicit definition of the kinetic energy term based on the Kohn-Sham orbitals:

$$T_s = -\frac{1}{2} \sum_i \langle \phi_i | \nabla^2 | \phi_i \rangle. \quad (2.18)$$

total (electronic) energy in the Kohn-Sham formulation:

$$E[\rho] = T_s[\rho] + E_{eN}[\rho] + J[\rho] + E_{xc}[\rho], \quad (2.19)$$

where $J[\rho]$ is the expression of the classical Coulomb repulsion (including a self-interaction):

$$J[\rho] = \frac{1}{2} \iint \frac{\rho(r_1)\rho(r_2)}{|r_1 - r_2|} dr_1 dr_2, \quad (2.20)$$

where $E_{eN}[\rho]$ is the energy of the electrons interacting with the external potential (from nuclei):

$$E_{eN}[\rho] = \int V_{ext} \rho(r) dr \quad (2.21)$$

and where E_{xc} is the exchange-correlation functional defined as:

$$E_{xc}[\rho] = (T[\rho] - T_s[\rho]) + (V_{ee}[\rho] - J[\rho]). \quad (2.22)$$

E_{xc} contains differences in kinetic energy and electron interaction energy arising from the approximate expressions in the T_s and J functionals. E_{xc} is formally exact but the functional form is unknown, while other terms are approximate but the functional forms are known. The KS energy and orbitals are determined variationally by minimization with respect to the density $\frac{\delta E}{\delta \rho} = 0$ and with respect to the individual Kohn-Sham orbitals $\frac{\delta E}{\delta \phi} = 0$. The non-interacting kinetic energy term (T_s) and an “effective potential” that depends purely on the density forms the Kohn-Sham equivalent of the Fock operator in HF and the corresponding pseudo-eigenvalue equation allows for determining the Kohn-Sham orbitals:

$$\left[-\frac{1}{2} \nabla^2 + v_{ext} + v_{coul} + v_{xc} \right] \phi_i = \epsilon_i \phi_i. \quad (2.23)$$

Here $v_{ext} = -\sum_{i,A} \frac{Z_A}{|r_i - R_A|}$ and $v_{coul} = \int \frac{\rho(r_2)}{|r_1 - r_2|} dr_2$ comes from the derivative of E_{eN} and $J[\rho]$ with respect to the density of $\rho(r_1)$. Similarly, exchange-correlation potential v_{xc} is introduced as:

$$v_{xc} = \frac{\delta E_{xc}}{\delta \rho}, \quad (2.24)$$

the functional derivative of E_{xc} . In KS-DFT, the central point is the determination of E_{xc} .

To determine a functional form of E_{xc} , a systematic approach begins with a simple model of the density and adds more complexity to better approximate E_{xc} (referred to as a “Jacob’s ladder” approach). This approach begins with the simplest approximation of evaluating the E_{xc} functional as an integral of local energies that are simply functions of the local density at each point, termed the *local density approximation* (LDA). LDA functionals are the most crude approximation to E_{xc} the functionals used in this thesis begin at higher “rungs” on this ladder. The first extension on the LDA approximation is to include corrections coming from the local gradient of the density ($\nabla \rho$) termed the *generalized gradient approximation* (GGA). In this thesis, the BP86 and BLYP GGA functionals are used primarily in determining the DFT energies for the liquid molecular dynamics simulations. A higher order approximation is done by including HF exchange to give the hybrid functionals. The TPSSh functional has been extensively used in this thesis for optimizing all of the isolated metal complexes. This is primarily because TPSSh has been demonstrated to provide accurate bond lengths and angles in comparison to empirically determined values. [32]

2.2.4 Coupled cluster theory

The coupled cluster description of the ground state wavefunction is expressed as an exponential cluster operator ($e^{\hat{T}}$) acting on a reference wavefunction (typically the HF wavefunction, denoted Φ_0):

$$|\psi\rangle = e^{\hat{T}} |\Phi_0\rangle \quad (2.25)$$

The cluster operator \hat{T} generates excitations from the reference wavefunction Φ_0 according to excitation order (1, 2, ..., N):

$$\hat{T} = \hat{T}_1 + \hat{T}_2 + \dots + \hat{T}_N = \sum_{a,i} c_i^a \Phi_i^a + \sum_{ab,ij} c_{ij}^{ab} \Phi_{ij}^{ab} + \dots \quad (2.26)$$

where N denotes the number of electrons. The total cluster operator (\hat{T}) is expanded in terms of the excitation operators ($\hat{T}_1 + \hat{T}_2 + \dots + \hat{T}_N$) and the corresponding cluster coefficients ($c_{i,\dots}^{a,\dots}$) termed cluster amplitudes. The coupled cluster ground state energy (E_{CC}) is obtained by projection of the inverse of the exponential operator and the electronic Hamiltonian onto the exponential ansatz in Eq. 2.25:

$$e^{-\hat{T}} \hat{H}_e e^{\hat{T}} \Phi_0 = E_{CC} \Phi_0. \quad (2.27)$$

The cluster amplitudes are similarly obtained by projection onto a space by excited determinants:

$$\langle \Phi_{ij,\dots}^{ab,\dots} | e^{-\hat{T}} \hat{H}_e e^{\hat{T}} \Phi_0 \rangle = 0 \quad (2.28)$$

Without truncation, the exponential ansatz is formally equivalent to the full CI expansion. At a given level of truncation *e.g.* single doubles truncation, the coupled cluster ansatz by definition includes more correlation to *any* order of truncation. For example, combinations of doubly excited determinants (Φ_{ij}^{ab}) results in quadruple, hextuple and higher order excitations.

A common truncation in coupled cluster is CCSD(T), where the (T) denotes that the triples contribution is estimated by many-body perturbation theory. [55] Despite this approximation, the CCSD(T) wavefunction scales by N^7 for the number of basis functions. For metal complexes with an appropriate basis set *e.g.* Fe(CO)₅ using the def2-TZVP basis, these computations are prohibitive. Recently, computational efficiency has been accomplished by the domain-based local pair natural orbital (DLPNO) variant

of the standard CCSD(T). Here localized molecular orbitals are expressed in terms of a pair density matrix spanned by the pair densities of the orbitals. The matrix that is diagonalized produces the “pair-natural orbitals” (PNOs) [35] with occupation numbers and coefficient weights. By discarding PNOs with a low coefficient weight, the CCSD(T) expansion can be significantly reduced in size. In **Paper III** and **IV**, the DLPNO-CCSD(T) variation is extensively used in order to provide benchmark energies of the metal complexes and their isomers.

2.2.5 Summary of electronic structure methods

In the preceding sections, a formal introduction of the electronic structure methods have been presented. It is worth stating the usability of each method as they pertain to molecular dynamics simulations and the calculation of experimental observables. Table. 2.1 provides a summary of the use of each electronic structure method in this thesis.

	energies	gradients	MD
HF (CASSCF, NEVPT2)	✓	✓	✓(with approximations)
DFT	✓	✓	✓(with approximations)
CCSD (DLPNO, (T))	✓	✗	✗

Table 2.1: Summary of the electronic methods employed in this thesis along with the applicability of each method.

The basic requirement fulfilled by all electronic structure methods used in this thesis is that they provide ground state energies. It is, however, not guaranteed that all methods are capable of providing excited state energies or gradients based on those energies within the framework of the quantum chemistry codes used. In this thesis the general workflow of the isolated complexes (*i.e.* a single metal complex without solvent) involves optimization with the TPSSh exchange-correlation functional. Using TPSSh optimized structure, we often need to understand the degree of multiconfigurational character with CASSCF and obtain benchmark energies within the DLPNO-CCSD(T) framework. In the molecular dynamics simulations, the expensive CASSCF, NEVPT2 and TDDFT energies and gradients are used for the isolated gas-phase simulations. For the liquid simulations, DFT is exclusively used in this thesis.

2.3 Nuclear Motion

In the description of the total wavefunction in Eq. 2.1, the nuclear and electronic degrees-of-freedom were factorized (Eq. 2.4) in order to approach the problem of finding solutions to Eq. 2.1. As a basis for the Born-Oppenheimer approximation, it was assumed that given the large mass difference between the electrons and nuclei, their motions would occur on different timescales. This was because of the Born-Oppenheimer expansion and definition of the electronic Hamiltonian, which made it possible to calculate potential energy surfaces at fixed nuclear geometries. Based on this ansatz and the potential energy surfaces derived from varying the nuclear geometry, it would also be possible to evolve a nuclear wavefunction to account for nuclear quantum effects. However, for large nuclei, the nuclear quantum effects are small relative to thermal effects at ambient temperatures.

In the molecular dynamics methods used in this thesis, the nuclei motion is governed by a numerical integration of Newton's equations-of-motion, evolving according to the gradient of the electronic potential energy surfaces. The distinction is made here between the two dynamics methods employed in this thesis: ground state molecular dynamics (GSMD) evolving on a single adiabatic potential energy surface and excited state molecular dynamics (ESMD) evolving on an arbitrary excited state adiabatic potential energy surface with non-adiabatic couplings mediating dynamics between surfaces. In the GSMD simulations employed here, a periodic liquid-phase system is evolved to study liquid dynamics in equilibrium. In the ESMD simulations employed here, a single molecule is evolved to study non-equilibrium gas-phase dynamics.

2.3.1 Ground state molecular dynamics

Ground state molecular dynamics (GSMD) involves the dynamics of a molecular system in the electronic ground state. There are few ingredients that are needed to simulate a molecular system of N -atoms for a time t . The basic structure of a GSMD simulation is illustrated in the following scheme:

For large molecular systems, the calculation of the potential energy surface and forces that guide the nuclei present the computational bottleneck in the simulation. To date, this has been circumvented by a *molecular mechanics* (MM) approach [12; 19] which derives functional forms of the intra- and inter-molecular potential energies between atoms in molecules. The potential energy is expressed as the sum of parameterized potential energy functions of the bonds, angles, torsions and non-bonded pairs in

Algorithm 1 Basic MD algorithm adapted from Ref. [28]

```
call init()                                ▷ Initialize position and momenta (R, p)
while  $t_0 < t < t_{final}$  do
    call energy()                          ▷ Calculate the potential energy  $E_{pot}$ 
    call force()                            ▷ Calculate the forces from potential energy  $-\frac{dE}{d\mathbf{R}}$ 
    call integrate()                        ▷ Integrate Newton's equations-of-motion.
     $t = t + \Delta t$                         ▷ Take step forward in time.
end while
```

the form of a “force field” library. The functions and parameterizations are determined empirically or from high-level electronic structure calculations. These approaches are computationally efficient, applicable to a variety of system sizes (single molecules to proteins) and because of the reduced cost can be used to propagate a molecular dynamics simulation from the picosecond to microsecond timescale. [12; 19] While these methods are amenable to many system sizes and timescales, the parameterization prevents a universal approach for bonding between atoms that are not known *a priori*. In the following section, we consider molecular dynamics simulation with energies and forces determined from electronic structure methods, termed “*ab initio*” molecular dynamics (AIMD).

Ab initio MD

In an AIMD simulation, electronic structure calculations are performed at each time step to determine the ground state energy and derive the forces that guide the nuclei. Restricting the dynamics to the an arbitrary adiabatic electronic state results in Born-Oppenheimer molecular dynamics (BOMD). The BOMD energies are obtained from the electronic structure calculations by solving the time-independent Schrödinger equation in Eq. 2.5, while the nuclei are evolved classically. Hence the calculation of the PES is done for each nuclear displacement in time. While it is beneficial to have more accurate PESs obtained from electronic structure, BOMD suffers from computational costs due to computational scaling with the number of particles. Furthermore, since the energy is minimized for Eq. 2.5 at each nuclear displacement, BOMD suffers from a global energy drift when the electronic structure does not converge properly [1; 46].

An alternative, Car-Parrinello MD (CPMD) [13] has been used which does not fully converge the electronic wavefunction at each timestep. Instead the wavefunction is converged at the first time step and the orbital coefficients are evolved as classical variables. This allows the wavefunction to be approximately optimized along the trajectory without having to do

the SCF iterations. The formulation of CPMD is done by using a plane wave (PW) basis and pseudopotentials in DFT. The PW basis has typically been applied to periodic systems such as metals and crystal lattices, however, because of the periodic nature of the GSMD simulation using periodic boundary conditions (PBCs), the PW basis is used. The CPMD algorithm is accomplished by including fictitious masses for the electronic degrees of freedom. If the fictitious mass is small, a very small timestep is needed but a good accuracy in the wavefunction is obtained. Increasing the fictitious mass is needed in order to be able to use large time steps, however, if fictitious masses approach that of the nuclei, the large temperature difference between the nuclei and coefficients breaks down and the previously optimized wavefunction is no longer optimized. In effect it provides a separation between the two degrees of freedom (electronic and nuclear) resulting in the adiabatic energy. [9] We use CPMD to perform the MD simulations in **Paper V** and **Paper VI**.

2.3.2 Excited state molecular dynamics

In excited state molecular dynamics (ESMD) the relative energies and crossings of ground and excited state PESs determine the outcome of a photochemical or photophysical reaction. Unlike GSMD, there are points in which surfaces cross and the non-adiabatic couplings (Λ_{ji}) from Eq. 2.8 become large. This coincides with the breakdown of Born-Oppenheimer approximation when nuclear motion on different potential energy surfaces is coupled. The result is a non-radiative process that acts as a “funnel” to mediate population transfer between the adiabatic electronic states. To understand when these non-radiative processes occur and the mechanisms that lead to population transfer, an ESMD simulation is needed. For this we consider the surface hopping algorithm detailed in the forthcoming section.

The Surface Hopping Algorithm

The surface hopping algorithm is referred to as a semi-classical approach whereby the nuclei are treated classically, evolving according to Newton's equations-of-motion and the electronic degrees-of-freedom are calculated by electronic structure methods. Additionally, a set of electronic coefficients are propagated so that they can be used to determine the hopping probability between electronic states. A popular implementation of the surface hopping algorithm is the *fewest switches surface hopping* (FSSH) algorithm [67] which makes use of a fixed number of trajectories that are propagated in time. The initial set of trajectories are independently propagated, obtaining electronic structure information *on-the-fly* and stochastically hopping between PESs when the coupling becomes large. The criteria for the hopping probability uses the electronic coefficients to evaluate a random number generator and screen the hop to another state. The basic algorithm for the FSSH in Algorithm 2 is similar to the GSMD Algorithm 1.

In the *energy()* and *force()* routines, these follow from the electronic structure calculation and the gradient routines in the program. The coupling is more difficult to define since many methods do not have analytic solutions for the *non-adiabatic* couplings defined in Eq. 2.8. This is true for excited state energies based on a linear response of the ground state DFT energy *i.e.* time-dependent DFT (TDDFT). To address this, consider first the representation of the electronic wavefunction in the FSSH ansatz:

$$|\psi(\mathbf{r}, t; \mathbf{R})\rangle = \sum_i c_i(t) |\psi_i(\mathbf{r}; \mathbf{R})\rangle \quad (2.29)$$

where $c_i(t)$ are the time-dependent coefficients multiplying each basis state

Algorithm 2 Basic surface hopping algorithm

```
call init()                                ▷ Initialize position and momenta (R,p)
while  $t_0 < t < t_{final}$  do
  call energy()                            ▷ Calculate the energies ( $E_i$ )
  call force()                             ▷ Calculate forces from potential energy  $-\frac{dE_i}{d\mathbf{R}}$ 
  call coupling()                          ▷ Calculate couplings
  call coeff()                             ▷ Determine electronic coefficients for the active state  $E_i$ 
  call hop()                               ▷ Determine hopping probability
  if hop() = True then
    Hop from  $E_i$  to  $E_j$ 
  else
    Remain on  $E_i$ 
  end if
  call integrate()                         ▷ Integrate Newton's equations-of-motion.
  call update()                             ▷ Update electronic coefficients for the active state  $E_i$ 
   $t = t + \Delta t$                          ▷ Take step forward in time.
end while
```

function $\psi_i(\mathbf{r}; \mathbf{R})$ which are chosen to be the adiabatic electronic states from an electronic structure calculation. In FSSH the coefficients are solved by inserting Eq. 2.29 into the TDSE to obtain:

$$\frac{\partial}{\partial t} c_j = - \sum_i \left[\frac{i}{\hbar} H_{ji} + K_{ji} \right] c_i \quad (2.30)$$

The H_{ji} return the adiabatic potential energy surface matrix elements, while the K_{ji} are the coupling matrix elements, typically taken to be the non-adiabatic couplings Λ_{ji} . To obtain the coefficients $c(t + \Delta t)$, Eq. 2.30 is integrated with respect to time.

The solution of the coefficients is necessary because of their use in determining the hopping probability, however, since many methods cannot calculate the couplings, approximations are made. For this the *wavefunction overlap* (WO) method has been chosen to approximately obtain the Λ_{ji} from wavefunction overlaps [50]:

$$K_{ji}(t + \Delta t) \approx \frac{1}{2\Delta t} (\langle \psi_j(t) | \psi_i(t + \Delta t) \rangle - \langle \psi_j(t + \Delta t) | \psi_i(t) \rangle) \quad (2.31)$$

The wavefunction overlap has been used in **Paper I and II** for FSSH dynamics simulation with energies and gradients from TDDFT. The term *fewest switches* was introduced so that the hopping does not occur too frequently.

If the electronic coefficients do not change, then the trajectory does not hop. However, if the coefficients change at the next time step, then the

probability to hop is given by:

$$p_{i\rightarrow}(t) = 1 - \frac{|c_i(t + \Delta t)|^2}{|c_i(t)|^2} \quad (2.32)$$

2.4 Spectroscopy

The theoretical understanding of the reactivity of $\text{Fe}(\text{CO})_5$ in this thesis is motivated by current experimental collaboration and the established experimental body of work. We often attempt to relate the insights gained from electronic structure calculations and molecular dynamics simulations to real chemical systems via the calculation of experimental probes. In the forthcoming section, the essential concepts of X-ray spectroscopy and photoelectron spectroscopy are introduced so that the theoretical contribution to the experimentally driven studies in **Paper II** and **Paper IV** can be detailed later.

2.4.1 Spectroscopic probes

The core-level excitations are classified by which core-orbital the incoming X-ray photon interacts with. Excitations are grouped according to the principle quantum number n , which for $n = 1, 2, 3, 4$ is denoted the K, L, M, N-edges. [6] For $n=1$ there is only the $1s$ core orbital and the orbital angular momentum $l=0$, therefore, all $1s$ orbitals are given the strict letter K. For lower binding energy core-orbitals such as the $n=2$, with values of $l=0, 1$, the $2s$ and $2p$ orbitals give the L_1 ($2s$), L_2 ($2p_{1/2}$) and L_3 ($2p_{3/2}$), respectively. The subscripts on the $2p$ denote the L-S or Russel Saunders coupling arising from the spin-orbit coupling (SOC) of the intrinsic spin ($+1/2, -1/2$) of the electron and the orbital angular momentum components. [5] This corresponds to $L=1$ and $S=+1/2, -1/2$ which yield $J = |L - S|$, $L+S$ of $1/2$ and $3/2$. The same rules apply to the M and N-edges, however, only the K and L-edges are employed in spectroscopic probes in this thesis. Based on the defined excitation levels, X-ray spectroscopic processes can be classified in terms of whether the incoming or “incident” photon results in a core excitation or a core-ionization.

X-ray absorption spectroscopy:

In the following section, the differences between the spectroscopic methods are detailed beginning with X-ray absorption spectroscopy (XAS). [64] Fig. 2.2(a) shows the basic XAS scheme.

In XAS, a resonant excitation occurs when the incident photon energy matches the gap electronic states, associated with a transition between a core-orbital and an unoccupied valence orbital below the continuum or the excitation goes into the continuum. This gives information about the orbital occupancies (oxidation states) in the valence molecular orbitals and spin state information. The excitation of an electron to an unoccupied valence orbital results in a core-hole state which is highly unstable due to the absence of an electron in the core orbital. The core-hole broadening (Γ_f) re-

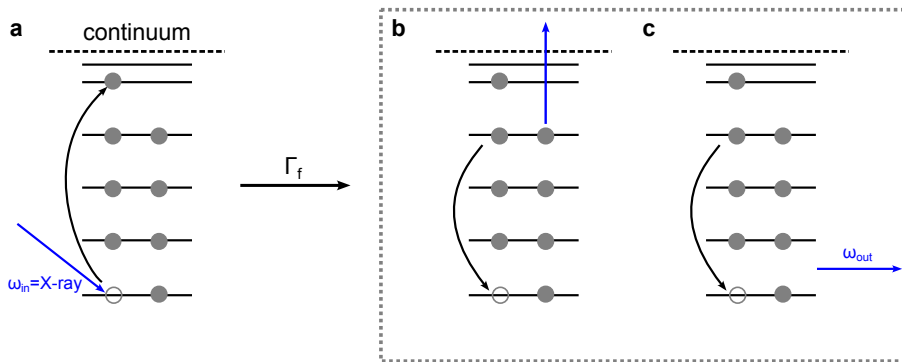


Figure 2.2: (a) A core orbital absorbs an X-ray photon (ω_{in}) which excited it to a unoccupied valence orbital below the continuum. (b) the core-excited state decays via an Auger-Meitner process which results in the filling of the core-orbital and the ejection of an electron from a higher l orbital. (c) the core-excited state decays via the filling of the core-orbital by a valence electron. The result is the emission of a photon of light (ω_{out}).

lated to the lifetime of the core hole state is short e.g. 4 fs for the O K-edge in CO or 11 fs for the Fe L_3 -edge in atomic iron. [6] This means that the core-hole state decays rapidly by a valence-electron falling down into the core-orbital and does so via two pathways: ejection of a secondary photoelectron by an Auger-Meitner process Fig. 2.2(b) or by fluorescence. For low Z elements, the process of Auger-Meitner decay dominates and occurs when an valence electron fills the core-hole, resulting in the ejection of a secondary electron. For higher Z elements, fluorescence dominates with the emission of a photon.

To obtain the XAS spectra, a spectrum of wavelengths are scanned and the absorption coefficient $\epsilon(\omega)$ is measured according to the Beer-Lambert Law:

$$A(\omega) = \epsilon(\omega)cd = \ln\left(\frac{I_0}{I_T}\right). \quad (2.33)$$

$A(\omega)$ is the *absorbance* which measures the absorption of monochromatic light by the sample of concentration c and with path length d . In doing so, the absorbance relates the attenuation of light through the sample to the properties of the sample. [65] What is measured is the incident X-ray signal (I_0) and the transmitted X-ray signal (I_T) after passing through the sample. In the case of the experiments in this thesis, the sample includes both the metal complex and the solvent. The total absorption coefficient $\epsilon(\omega)$ is calculated by Fermi's Golden Rule:

$$\epsilon(\omega) \approx \sum_f |\langle f | \hat{H}_{int} | i \rangle|^2 \times \frac{\Gamma_f/2\pi}{(E_f - E_i - \hbar\omega)^2 + \Gamma_f^2/4} \quad (2.34)$$

For a set of final states $\langle f |$, the transition from the initial state is determined. The final states $\langle f |$ have energy E_f , the initial state $|i\rangle$ has energy E_i and the incident X-ray has energy $\hbar\omega$. The final state (the core-hole excited state) has a finite lifetime with the core-hole broadening Γ_f described above. The transition from the initial state to final state is described by the interaction Hamiltonian \hat{H}_{int} approximated by the dipole approximation (typically sufficient for soft X-rays) or a higher order approximation like the dipole-quadrupole approximation.

For the transition to be allowed, the angular momentum must change by $\Delta l = \pm 1$. With metal complexes involving the d-orbitals, excitation from the $1s \rightarrow 3d$ ($\Delta l = 2$) is forbidden in the dipole approximation but allowed within the dipole-quadrupole approximation. For the metal $2p \rightarrow 3d$ L-edge spectroscopy used in the experiments presented in this thesis, the change in angular momentum is $\Delta l = \pm 1$. These allowed L-edge transitions have a greater intensity but also offer a better resolution due to a smaller core-hole lifetime broadening when compared to the metal K-edge spectra. [21]

Instead of measuring the transmission signal (I_T), the secondary processes of Auger-Meitner and fluorescence Fig. 2.2(b) and Fig. 2.2(c), respectively, can be measured. In Auger-Meitner decay in Fig. 2.2(b), the outgoing photoelectron scatters off nearby electrons, resulting in the ejection of a secondary electron. The outgoing electrons are measured and give a total electron yield (TEY) which can be used as an indirect and approximate measure of the transmission XAS signal, which for many systems is more challenging to measure directly. In the fluorescence decay in Fig. 2.2(c), the filling of the core-hole results in the emission of a photon which can be measured in the total fluorescence yield (TFY), another indirect measure of XAS. For this process, there exists an intermediate state (n) decays to the final valence-excited state. Here the scattering cross section is given as a sum of all of the intermediate state probabilities by a modified Kramers-Heisenberg formula:

$$F(\omega_{in}, \omega_{out}) = \frac{\omega_{out}}{\omega_{in}} \sum_f \left| \sum_n \frac{\langle f | \hat{H}_{int} | n \rangle \langle n | \hat{H}_{int} | i \rangle}{E_n - E_i - \hbar\omega_{in} - i\Gamma_n} \right|^2 \times \frac{\Gamma_f/\pi}{(E_f - E_i - \hbar(\omega_{in} - \omega_{out}))^2 + \Gamma_f^2} \quad (2.35)$$

Here $|n\rangle$ denotes the intermediate state (core-excited state) with an associated intermediate state lifetime Γ_n .

In the time-resolved experiments that are presented in this thesis, the transmission XAS intensity (I_T) were recorded for the picosecond timescale reactions probed by synchrotron generated X-rays. In the short timescale reactions in **Paper A**, the TFY were recorded. In order to probe photoinduced reactions by time-resolved experiments, the intensity is measured as a function of time ($\Delta A(\omega, t)$) according to the following equation:

$$\Delta A(\omega, t) = f \cdot [\Phi(t)I_{pumped}(\omega) - I_{unpumped}(\omega)] \quad (2.36)$$

where f is the fractional population of the excited state, often called the photolysis yield. [10] The photolysis yield is important because it determines the total fraction of initially excited molecules. It is dependent on the total absorption coefficient, $\epsilon(\omega)$ from Eq. 2.33, since the magnitude of $\epsilon(\omega)$ is related to the probability of an electronic excitation occurring. The first time-dependent quantity is the quantum yield of the product, $\Phi(t)$, which determines the fraction of the excited molecules which go on to form the photoproduct. In the time-resolved experiment, the intensity of the pumped sample ($I_{pumped}(\omega)$) and of the unpumped sample ($I_{unpumped}(\omega)$) are recorded to determine the subsequent photoinduced dynamics.

Photoelectron spectroscopy:

Photoelectrons have already been discussed in the context of the Auger-Meitner decay of the core-excited state. However, this process occurs directly if the photon energy is high enough to overcome the work function of the material. This is the photoelectric effect:



which yields an ejected electron (e^-) from a neutral system (X) and produces an ionized system (X^+). Expressing the above process in terms of the energy results in the typical notation involving the binding energy (BE) of the electron:

$$KE = h\nu - [E(X^+) - E(X)] = h\nu - BE \quad (2.38)$$

The name of the photoelectron spectroscopy (PES used in this context, not to be confused with potential energy surface) technique is defined by the source wavelength of the incident photon, $h\nu$. For example, wavelengths

from an X-ray source (XPS) (10-1 nm), an extreme-ultraviolet (XUV-PES) (<100 nm) or from the vacuum ultraviolet (VUV-PES) (100-200 nm).

In **Paper II**, a an XUV pulse is used to generate photoelectrons following an initial photoexcitation by a pump laser pulse. This photoelectron spectroscopy “probe” can be used to learn about the evolution of the molecule in the excited state. This is generalized for an arbitrary set of neutral and ionized excited states in Fig. 2.3.

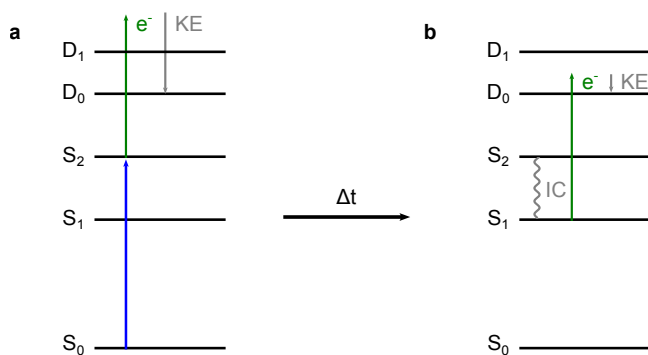


Figure 2.3: (a) A pump pulse excites the system to the S_2 excited state. A probe pulse ionizes the neutral molecule by exciting the molecule to the lowest cationic state, D_0 , where the excess energy results in the photoelectron kinetic energy (KE). (b) Following internal conversion (IC), the excited molecule non-radiatively decays to S_1 . The probe interacts with the S_1 state by exciting the molecule to the lowest cationic state, D_0 , which results in a shift of the photoelectron kinetic energy.

An initial pump laser pulse photoexcites a molecule to an excited state (here S_2) that evolves in time, changing the potential energy, position and momenta of the molecule in that state. The probe pulse capable of ionizing the molecule (e.g. XUV) ionizes an electron from the excited state generating a the first cationic state (here D_0). The difference in the probe energy and the cationic state energy determines the kinetic energy of the photoelectron. If internal conversion (IC) occurs in the excited state, the molecule transfers excited state population to an excited state or to the electronic ground state. In Fig. 2.3, the IC to S_1 results in a shift in the kinetic energy of the photoelectron the first cationic state is generated (here D_0). This method is generally termed time-resolved photoelectron spectroscopy (TRPES) [63] and often referred to as time-resolved photoemission spectroscopy due to the emission of a photoelectron. This is the case in **Paper II**, where we probe the lowest cationic state, corresponding to the ejection of an electron from the highest occupied molecular orbital.

From a computational perspective, the photoelectron spectra generated by

the probe pulse can be simulated using some of the aforementioned electronic structure methods. In **Paper II**, the photoelectron spectra are calculated for the ground and excited electronic states using CASPT2, where the valence neutral and cationic states are calculated individually. The probabilities of ionization are approximated as the squares of the Dyson orbital norms ($||\phi_{i\alpha}^D||^2$):

$$\phi_{i\alpha}^D = \sqrt{N} \int \psi_{\alpha}^{N-1}(\mathbf{r}_2, \mathbf{r}_3, \dots, \mathbf{r}_N) \psi_i^N(\mathbf{r}_1, \mathbf{r}_2, \mathbf{r}_3, \dots, \mathbf{r}_N) d\mathbf{r}_2 d\mathbf{r}_3 \dots \mathbf{r}_N. \quad (2.39)$$

The squares of the Dyson orbital norms weigh the calculated transitions between the neutral and cationic state. Along with the probe pulse energy, they determine the photoelectron kinetic energy.

3. Summary of results

In the subsequent summary we first address the questions concerning the short time dynamics in **Paper I** and **Paper II** in the gas-phase. In the second part of the summary, we address questions concerning the long time dynamics of $\text{Fe}(\text{CO})_5$ from a theoretical perspective in **Paper III**. In the third part of the summary, we provide a series of joint theoretical and experimental studies (unpublished work and **Paper IV**), beginning with a time-resolved Fe L-edge study to elucidate the photoproduct dynamics. In the final part, we summarize **Paper V** and **Paper VI** where we present the structure and dynamics of an additional iron complex that is defined by large multiconfigurational effects in its electronic ground state.

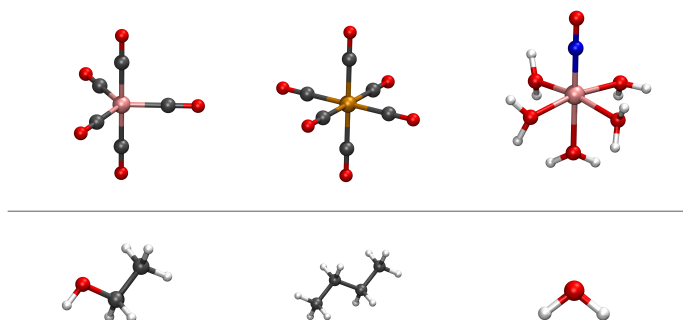
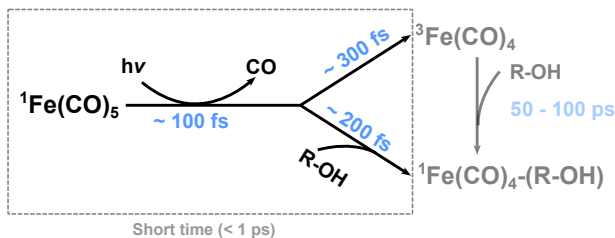


Figure 3.1: The transition metal complexes studied in this thesis (top) along with corresponding solvent molecules studied in relation to each complex (bottom). **Top:** ironpentacarbonyl ($\text{Fe}(\text{CO})_5$), chromiumhexacarbonyl ($\text{Cr}(\text{CO})_6$) and the “brown-ring” complex ($[\text{Fe}(\text{H}_2\text{O})_5(\text{NO})]^{2+}$). **Bottom:** ethanol ($\text{C}_2\text{H}_5\text{OH}$), butane (C_4H_{10}) and water (H_2O)

3.1 Short-time dynamics (< 1 ps)



As outlined in Sec. 1, we have chosen $\text{Fe}(\text{CO})_5$ as a model system to derive general insights into the structure and reactivity of metal carbonyls. The short time dynamics studied in this thesis builds on a library of experimental studies which have attempted to elucidate how the initial wavepacket dynamics of excited state $\text{Fe}(\text{CO})_5$ leads to the release of a CO. As shown in the scheme above, the release of a CO occurs rapidly (< 100 fs) leading to the production of $\text{Fe}(\text{CO})_4$ in a singlet or triplet state. In **Paper I and II** we used ESMD simulations to assign the mechanism that gives rise to CO release and in doing so we present a characterization of excited state potential energy surfaces that mediate population transfer in the excited state. To simplify the picture and simulations of the short time dynamics, we considered a gas-phase simulation of $\text{Fe}(\text{CO})_5$ and only in the singlet manifold.

3.1.1 Mechanistic insights into the $\text{Fe}(\text{CO})_5$ photodissociation process following excitation by 266 nm:

The gas-phase dynamics were simulated by the fewest-switches surface hopping (FSSH) method with the energies and gradients calculated by TDDFT with the CAM-B3LYP functional and the def2-TZVP basis. Fig.3.2 shows the frontier molecular orbitals of $\text{Fe}(\text{CO})_5$ which give the low-lying valence excited states. Since the carbonyl ligand is a neutral ligand (*i.e.* it does not change the formal oxidation state of the metal), $\text{Fe}(\text{CO})_5$ contains an Fe(0) metal with a d^8 occupation. This gives four filled 3d orbitals ($3e'$ and $10e''$) and an unoccupied 3d orbital ($14a_1^*$) with mixed $3d-\sigma_{\text{CO}}^*$ character. Higher energy unoccupied orbitals form with mixed π_{CO}^*-3d character.

The excitations from the set of occupied orbitals to the set of unoccupied orbitals are divided into two classes, the metal-to-ligand charge transfer (MLCT) states and the metal centered (MC) states, where the former give the optically bright transition in $\text{Fe}(\text{CO})_5$. These transitions are summarized in Tab. 3.1, corresponding to the TDDFT energies of the excited states. Underlying the optically bright S_6 MLCT state is a set of MC and MLCT

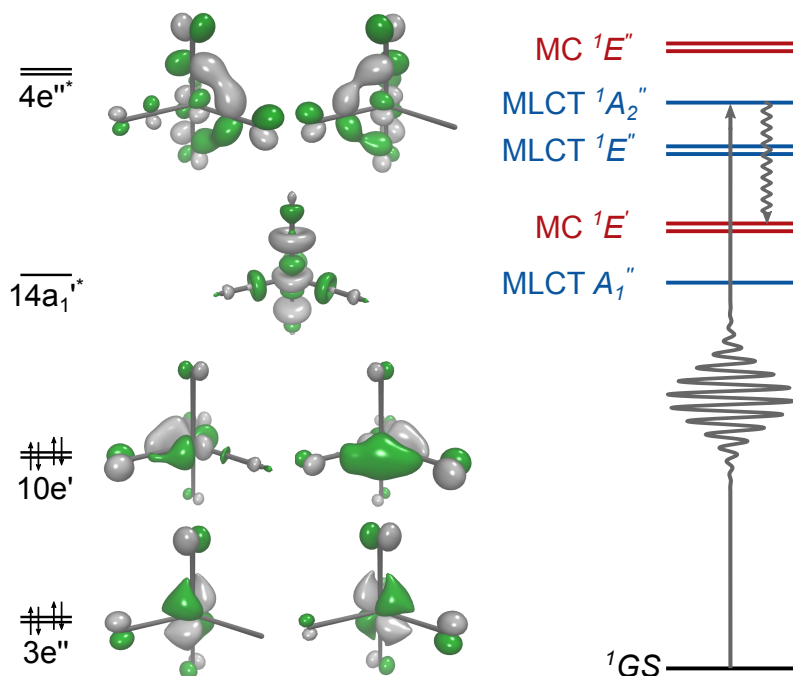


Figure 3.2: Frontier molecular orbitals of $\text{Fe}(\text{CO})_5$ that give rise to the valence electronic transitions. Transitions formed between the occupied 3d ($3e'$ and $10e''$) orbitals and the unoccupied π_{CO}^* -3d ($4e'^*$) orbitals result in the optically bright MLCT state being populated by a 266 nm pulse. The simplified mechanistic picture of the excited state decay is shown on the right. Adapted from **Paper I**.

states that are not populated in the Franck-Condon region. However, as shown in Fig. 3.2, the initially populated S_6 MLCT state is subject to decay to the lower MC states.

State	TDDFT (eV)	Osc. str.	Character
$^1A_1''$ (MLCT)	3.89	0.000	$10e' \longrightarrow 4e'^*$
$^1E'$ (MC)	3.97	0.000	$10e' \longrightarrow 14a_1'^*$
$^1E''$ (MLCT)	4.17	0.000	$10e' \longrightarrow 4e'^*$
$^1A_2''$ (MLCT)	4.40	0.067	$10e' \longrightarrow 4e'^*$

Table 3.1: The calculated CAM-B3LYP/def2-TZVP excited state energies of $\text{Fe}(\text{CO})_5$ at the optimized D_{3h} geometry.

To simulate this process, 116 trajectories were initiated in the optically bright S_6 MLCT state. The uncoupled trajectories were allowed to evolve for up to 600 fs, after which they were terminated. The couplings between the excited states were treated via a wavefunction overlap approach to approximate the nonadiabatic couplings.

Our results address a question of *whether the dissociation of $Fe(CO)_5$ occurs via an axial or equatorial CO mechanism*. We find that 110 of the 116 trajectories dissociate a single CO ligand, where 94 trajectories follow an axial mechanism and 16 follow an equatorial mechanism. We find that the initially excited molecules experience a symmetric stretching which elongates the already longer (0.1 Å) axial Fe-C distances, translating into a faster dissociation for the axial CO ligands. To translate this into a general mechanism, we consider the following scheme in Fig. 3.3

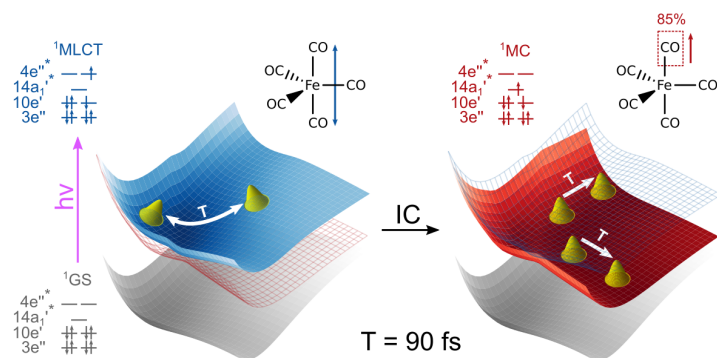


Figure 3.3: Oscillations in the metal-to-ligand charge-transfer (MLCT) state, coloured blue, and the periodic depletion of those states to metal-centered (MC) state of dissociative character, coloured red. Adapted from **Paper I**.

In Fig. 3.3, the potential energy surfaces are taken from the CAM-B3LYP/def2-TZVP calculations, plotted along the two axial Fe-C coordinates. The symmetric axial stretching of $Fe(CO)_5$ in the MLCT state results in periodic bursts of population transfer to the lower MC states (shown here as a single state). We find that on those states, either axial CO is capable of dissociating. We find that the population of the MC states are essential in causing the dissociation. This is because the lower MC states are formed by excitation from the occupied 3d orbitals into the unoccupied $14a_1^*$ orbital. This orbital is inherently anti-bonding with respect to the iron ($3d_{z^2}$) and CO (σ) orbitals. The result is a set of dissociative excited states that give release of a CO.

We examine this excited state reaction mechanism by considering all singly dissociating $Fe(CO)_5$ trajectories and tracking the Fe-C distances for all dissociating CO ligands. In Fig. 3.4(a-b), the Fe-C oscillations are shown as a

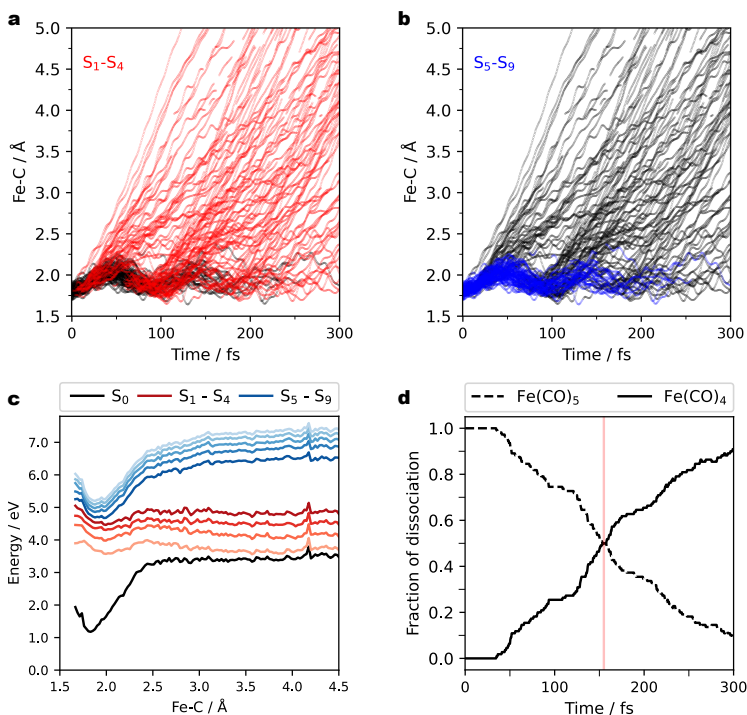


Figure 3.4: (a-b) The scatter plot of the Fe-C oscillations for all axially dissociating CO ligands. The scatter points indicate the data points originating from the (a) dissociative (red) and (b) bound (blue) states. (c) The average potential energies for all ground and excited states of $\text{Fe}(\text{CO})_5$ at each Fe-C distance for all axially dissociating CO ligands. (d) The fraction of $\text{Fe}(\text{CO})_5$ as a function of time based on the point of no return criteria of 2.5 Å for the axially dissociating CO ligands. A composite figure adapted from data in **Paper I** and **Paper II**.

function of time, while the red/blue scatter points show the state specific contributions to the Fe-C oscillations for the $S_1 - S_4$ and $S_5 - S_9$ adiabatic electronic states, respectively. In Fig. 3.4(a), the lower $S_1 - S_4$ states are shown to be dissociative, while in Fig. 3.4(b), the higher states are shown to be bound.

From each trajectory, we plotted the average potential energies for all adiabatic electronic states, at all times in Fig. 3.4(c). These average potentials provided an insight into the type of state: bound (blue) or dissociative (red), allowing for a general picture of bound oscillations leading to periodic population transfer to the lower dissociative states. Returning to Fig. 3.4(b), the red scatter plots for all of the bound states in Fig. 3.4(c) corroborate this view by showing that these states ($S_5 - S_9$) are indeed bound. Finally, we address the dissociation times of $\text{Fe}(\text{CO})_5$ by considering an ar-

bitrary threshold of dissociation. To do so, we performed a rolling average of the Fe-C oscillations to damp fast CO stretching modes and found that for all trajectories, the value of 2.5 Å was the point of no return for each dissociating Fe-C bond. We had to use a rolling average of the Fe-C distances since some distances passed the 2.5 Å threshold due to CO contractions coupled to Fe-C elongations, however, the molecules remained bound. By removing these fast oscillations, we were able to obtain the actual time at which the Fe-C distance reached a point of no return.

Using this measure of bond dissociation, the fraction of Fe(CO)_5 and Fe(CO)_4 is plotted in Fig. 3.4(d), where the semi-transparent red line indicates the point at which the populations are equal. We find an initial delay time of approximately 45 fs to be related to the synchronous axial Fe-C stretching in the bound ($S_5 - S_9$) excited states, followed by a prompt dissociation on the lower dissociative ($S_1 - S_4$) excited states.

3.1.2 Excited state dissociation times of $\text{Fe}(\text{CO})_5$ and $\text{Cr}(\text{CO})_6$ following excitation by 266 nm:

The analysis performed on the excited state dynamics of $\text{Fe}(\text{CO})_5$ provided a toolkit to study another well known and often compared system: chromiumhexacarbonyl or $\text{Cr}(\text{CO})_6$. It has been shown by Fuß et al. [30], that the excited state dynamics of $\text{Cr}(\text{CO})_6$ is considerably faster than $\text{Fe}(\text{CO})_5$ and has been attributed to a rapid IC to the MC states, involving Jahn-Teller distortions. [48] To date, the excited state dynamics using FSSH have been detailed by Barbatti et al., [20] using TDDFT to generate the potential energies and forces guiding the trajectories. There, they used the B3LYP functional and the TZVPP all electron basis set. To make an accurate comparison to $\text{Fe}(\text{CO})_5$, we reproduced their results using the CAM-B3LYP functional and the def2-TZVP basis set for the $\text{Cr}(\text{CO})_6$ surface hopping simulations.

Before the dynamics results can be discussed, it is meaningful to provide an overview of the orbitals and transitions involved in $\text{Cr}(\text{CO})_6$. Like $\text{Fe}(\text{CO})_5$, $\text{Cr}(\text{CO})_6$ contains a formally neutral metal atom $\text{Cr}(0)$, which in this case, has a d^6 occupation. As shown in Fig. 3.5, this results in triply degenerate occupied 3d orbitals ($2t_{2g}$) and the higher energy unoccupied 3d orbitals of $3d_{z^2}$ and $3d_{x^2-y^2}$ character (not shown). Lying between these occupied and unoccupied metal centered orbitals are sets of degenerate unoccupied orbitals of mixed π_{CO}^* -3d character. The lowest energy set of these are the $9t_{1u}^*$ unoccupied orbitals.

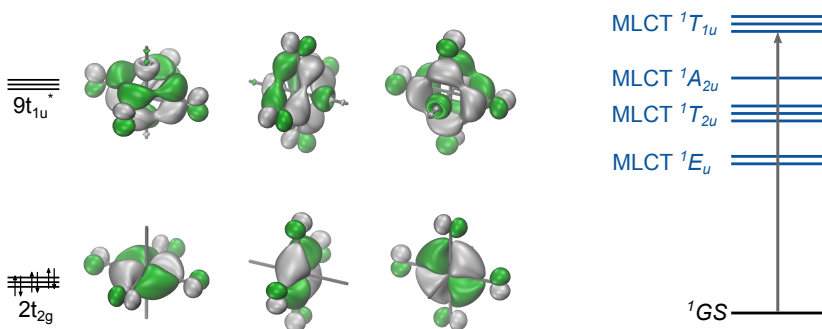


Figure 3.5: Frontier molecular orbitals of $\text{Cr}(\text{CO})_6$ that give rise to the valence electronic transitions.

The excitations formed between these sets of orbitals are exclusively described as MLCT states. These transitions are summarized in Tab. 3.2, corresponding to the TDDFT energies of the excited states. Unlike $\text{Fe}(\text{CO})_5$, there are no MC states underlying the triply degenerate optically bright $S_7 - S_9$ MLCT states. Instead, as mentioned, the rapid splitting of the states by Jahn-Teller distortions lowers the higher energy MC states which can

become populated outside of the Franck-Condon region (*i.e.* Cr-C elongations)

State	TDDFT (eV)	Osc. str.	Character
1E_u (MLCT)	4.339	0.000	$2t_{2g} \longrightarrow 9t_{1u}^*$
$^1T_{2u}$ (MLCT)	4.436	0.000	$2t_{2g} \longrightarrow 9t_{1u}^*$
$^1A_{2u}$ (MLCT)	4.465	0.000	$2t_{2g} \longrightarrow 9t_{1u}^*$
$^1T_{1u}$ (MLCT)	4.842	0.0243	$2t_{2g} \longrightarrow 9t_{1u}^*$

Table 3.2: The calculated CAM-B3LYP/def2-TZVP excited state energies of $\text{Cr}(\text{CO})_6$ at the optimized O_h geometry.

To simulate this process by FSSH simulations of $\text{Cr}(\text{CO})_6$, 88 independently evolving trajectories were initiated in the S_7 (44 trajectories) and S_8 (44 trajectories) optically bright MLCT states. We reproduce the analysis performed in Fig. 3.4 on $\text{Cr}(\text{CO})_6$ in Fig. 3.6.

In Fig. 3.6(a-b) we find a similar dynamics pathway outlined for $\text{Fe}(\text{CO})_5$, where the initially populated states ($S_7 - S_8$) are within a manifold of bound states that deplete population to the lower adiabatic states which are dissociative ($S_1 - S_3$). Like $\text{Fe}(\text{CO})_5$, we find Cr-C oscillations occurring on a period of 90 fs, however, unlike $\text{Fe}(\text{CO})_5$, the population to the lower dissociative electronic states is rapid, occurring largely within the first Cr-C oscillation. Upon inspection of the average potential energy surfaces in Fig. 3.6(c), we find a possible clear explanation for the rapid decay to be attributed to the small energetic gap between all of the states and between the group of bound ($S_4 - S_{11}$) and dissociative ($S_1 - S_3$) states. Since the coupling of the states via the non-adiabatic couplings in Eq. 2.9 has an inverse dependence on the gap between two electronic states, the dissociation of $\text{Cr}(\text{CO})_6$ is more rapid than $\text{Fe}(\text{CO})_5$, as evidenced by the Cr-C oscillations and in turn the fraction of population in Fig. 3.6(d). Here we find roughly the same initial delay time of approximately 45 fs before the first trajectories begin to dissociate. To determine the threshold for dissociation, we applied the same rolling average calculation for all dissociating Cr-C bonds and found that a threshold of 2.6 Å was the point of no return for each dissociating Cr-C bond. Given that the Cr-C distances of $\text{Cr}(\text{CO})_6$ are only 0.1 Å longer than the Fe-C distances of $\text{Fe}(\text{CO})_5$, the magnitudes of the oscillation are the same and occur on the same time period. We find the production of $\text{Cr}(\text{CO})_5$ to be significantly faster than for $\text{Fe}(\text{CO})_4$ as shown in Fig. 3.6(d), with the fraction of $\text{Cr}(\text{CO})_6$ and $\text{Cr}(\text{CO})_5$ becoming equal approximately 50 fs earlier.

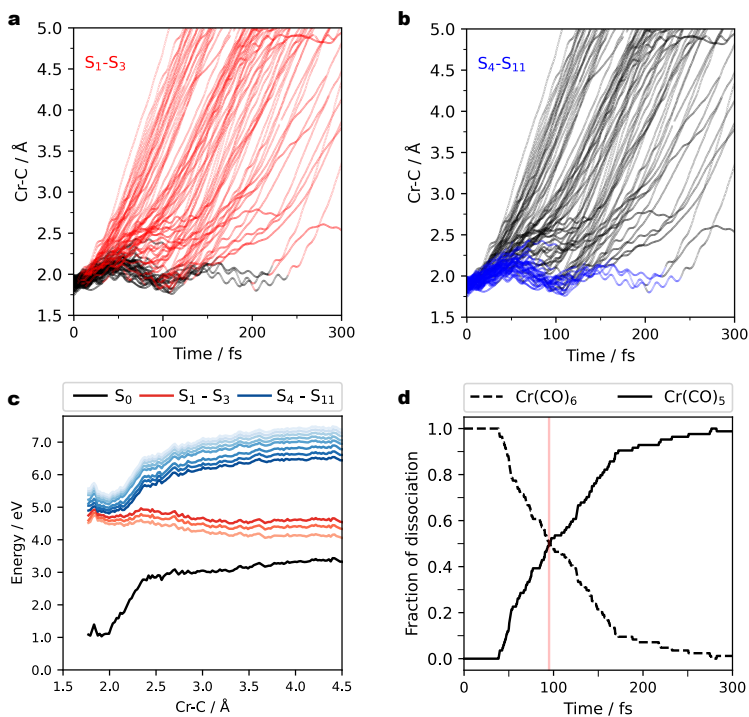


Figure 3.6: (a-b) The scatter plot of the Cr-C oscillations for all dissociating CO ligands. The scatter points indicate the data points originating from the (a) dissociative (red) and (b) bound (blue) states. (c) The average potential energies for all ground and excited states of Cr(CO)_6 at each Cr-C distance for all dissociating CO ligands. (d) The fraction of Cr(CO)_6 as a function of time based on the point of no return criteria of 2.6 Å for the dissociating CO ligands. A composite figure adapted from data in **Paper II**

3.1.3 Probing the excited state lifetimes of $\text{Fe}(\text{CO})_5$ and $\text{Cr}(\text{CO})_6$ by photoelectron spectroscopy

The previous sections provided us with a basic understanding of the inherent differences in the excited state dynamics of $\text{Fe}(\text{CO})_5$ and $\text{Cr}(\text{CO})_6$. Here we briefly detail the theoretical interpretation of the time-resolved photoelectron measurements in **Paper II**, while providing minimal information of the experimental results. In Fig. 3.7(a-b), the ground state photoelectron spectra are shown for $\text{Fe}(\text{CO})_5$ and $\text{Cr}(\text{CO})_6$, respectively. In both spectra, the lower binding energy peaks correspond to the highest occupied molecular orbitals of 3d character, followed by higher binding energy peaks corresponding to ionization from the ligand centered CO π orbitals. We note here that the spectra highlight the degeneracies of the Fe ($3e''$ and $10e'$) and Cr ($2t_{2g}$) orbitals.

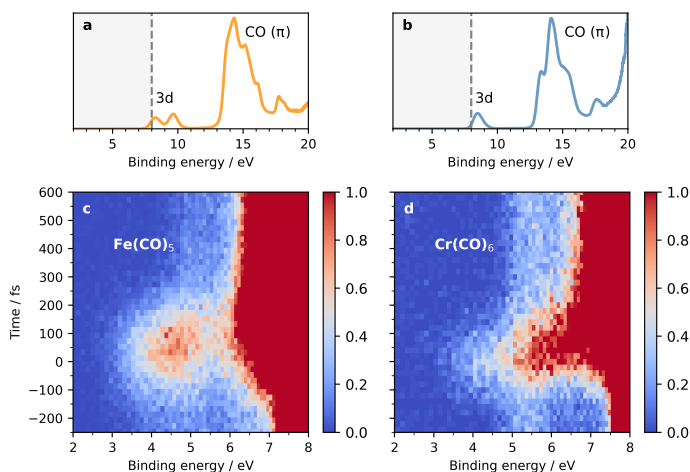


Figure 3.7: Measured steady-state and time-resolved valence photoelectron spectra of $\text{Fe}(\text{CO})_5$ and $\text{Cr}(\text{CO})_6$ in the gas phase. (a-b) Steady-state spectra of ground-state $\text{Fe}(\text{CO})_5$ and $\text{Cr}(\text{CO})_6$ with assigned metal 3d peaks (photoionization from metal 3d orbitals) and CO π peaks (photoionization from CO π orbitals). (c-d) Time-resolved pump-probe photoelectron intensities of $\text{Fe}(\text{CO})_5$ and $\text{Cr}(\text{CO})_6$ following photoexcitation at 266 nm as a function of pump-probe time delay and up to binding energies of 8 eV just below the metal 3d peaks of ground-state species (intensities encoded in color according to the given color bar, maximum intensities normalized to one by dividing intensities by 1×10^3 for $\text{Fe}(\text{CO})_5$ and by 1×10^4 for $\text{Cr}(\text{CO})_6$, photoelectron intensities at highest binding energies are saturated in this representation). Figure and caption adapted from **Paper II**.

The experimental TRPES for $\text{Fe}(\text{CO})_5$ and $\text{Cr}(\text{CO})_6$ are shown in Fig. 3.7(c-d). In these spectra, the difference is centered on the spectral evolution in the region between 4-6 eV, where for $\text{Fe}(\text{CO})_5$ this region persists for a

longer time relative to $\text{Cr}(\text{CO})_6$, as shown by the immediate decay at $t=0$ in the $\text{Cr}(\text{CO})_6$ spectrum. This region in the spectra corresponds to excited states which lower the binding energy of the highest occupied molecular orbital.

Our excited state dynamics indicated that there was a generality of the excited state potential energy surfaces that could be grouped into a manifold of bound excited states (coloured blue) and a manifold of dissociative excited states (coloured red). We summarize the potential photoionization process that occurs from each of these sets of states in Fig. 3.8. **Note:** the colour scheme in **Paper II** is reversed but we switch it here to make a direct comparison to the dynamics in **Paper I**.

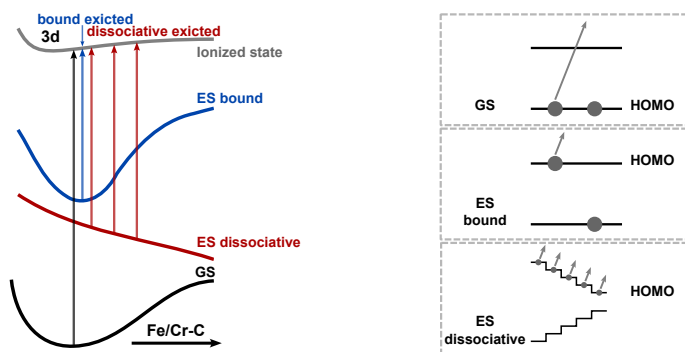


Figure 3.8: Schematic of the main photoionization processes and calculated photoelectron spectra of ground and excited states of $\text{Fe}(\text{CO})_5$ and $\text{Cr}(\text{CO})_6$. Left: Schematic depiction of ground state (GS), excited state (ES, bound and dissociative) and ionized-state potentials as a function of metal (M)-carbon (C) distance. Right: Simplified molecular-orbital energies and electron populations of ground and excited states (bound and dissociative) of $\text{Fe}(\text{CO})_5$ and $\text{Cr}(\text{CO})_6$ (HOMO and one higher-lying orbital, arrows indicate photoionization of the “active electron” in the highest-lying occupied molecular orbital). Figure and caption adapted from **Paper II**.

We briefly discussed the nature of the photoelectron spectrum defined in Sec. 2.4.1 as it pertains to the excited state dynamics. Here we find that all of the species have the same final state corresponding to the ionization of the photoelectron from either the ground state HOMO or from a formerly unoccupied orbital. In the right panel of Fig. 3.8 we summarize this effect as a shifting of the photoelectron kinetic energy as the excited state molecules undergo internal conversion from the higher bound states to the lower dissociative states. To quantify this, we considered a CASSCF wavefunction with an active space containing the occupied 3d orbitals and the low-lying unoccupied valence orbitals that possess $\text{CO}-\pi^*$ character. This corresponded to a CAS(10e,10o) wavefunction which we used as a refer-

ence in a subsequent CASPT2 calculation. For the lowest 10 singlet states and the first 100 doublet states, we simulated the photoelectron spectra of $\text{Fe}(\text{CO})_5$ and $\text{Cr}(\text{CO})_6$ shown in Fig. 3.9 with intensities of the transitions obtained from the Dyson orbital norms defined in Eq. 2.39.

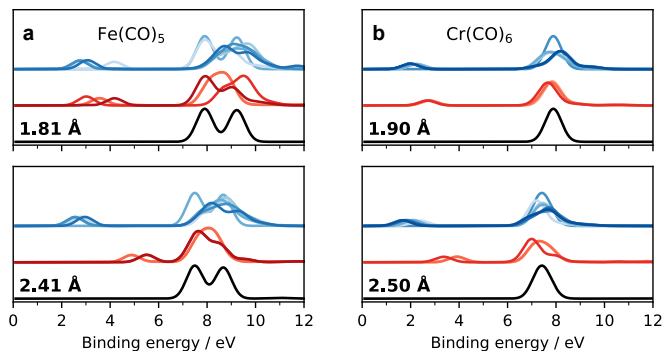
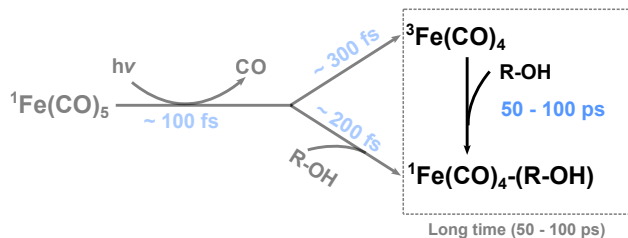


Figure 3.9: Calculated valence photoelectron spectra of ground states (black), bound excited states (red) and dissociative excited states (blue) of $\text{Fe}(\text{CO})_5$ and $\text{Cr}(\text{CO})_6$ for the indicated metal-carbon distances, plotted up to the 3d peaks of the ground-state species. Figure and caption adapted from **Paper II**.

In addition, we considered a two geometries from a rigid scan of the axial Fe-C carbonyl distance (Fig. 3.9(a)) and a Cr-C distance (Fig. 3.9(b)). These correspond to the equilibrium bond distances in the top panel and a 0.5 Å elongation of each bond. Our results show that as the bonds are elongated, the photoelectron kinetic energies decrease and the binding energies increase. These theoretical results map on to the findings from the experimental TRPES measurement, which despite the long time-resolution (180 fs FWHM pump-probe overlap), is capable of probing the presence of excited state dynamics in both complexes.

In a conclusion to the work, we find in **Paper II** that the excited state dynamics simulations and simulations of the photoelectron spectra offer important insights such as dissociation times, electronic populations and explanation of probes.

3.2 Long time dynamics (1 ps - 1 ns)



3.2.1 Photoproduct dynamics simulations of $\text{Fe}(\text{CO})_4$ in ethanol solution

The computational tools employed in this thesis cannot (presently) track the formation of $\text{Fe}(\text{CO})_4$ in the singlet and triplet states from $\text{Fe}(\text{CO})_5$. Instead, we investigate the photoproducts directly by means of AIMD simulations. To do so, we assume that these transient photoproducts which persist for some 50-100 ps are in a thermal equilibrium, with $\text{Fe}(\text{CO})_4$ in the singlet and triplet states having shed excess vibrational energy resulting from the initial excitation of $\text{Fe}(\text{CO})_5$. We performed the dynamics of $\text{Fe}(\text{CO})_5$, ${}^1\text{Fe}(\text{CO})_4$ and ${}^3\text{Fe}(\text{CO})_4$ to understand how the reactants and transient products are equilibrated in the bulk liquid.

Fig. 3.10(a) shows the radial distribution functions (RDFs) or $g(r)$ for the three simulations. By excluding the CO carbon and oxygen indices, we calculated the $g(r)$ for all iron and ethanol coordinations. Our results find that $\text{Fe}(\text{CO})_5$ is non-reactive with ethanol, as indicated by the lack of well defined structure in the $g(r)$. We find that ${}^1\text{Fe}(\text{CO})_4$ forms a tightly bound bond with an ethanol molecule via the hydroxyl (-OH) group, as indicated by the sharp peak in the $g(r)$. Finally, we find that ${}^3\text{Fe}(\text{CO})_4$ forms a weakly bound complex with an ethanol at a distance, as indicated by the broad but well defined peak centered around 3 Å. Fig. 3.10(b) shows the representative structures obtained from the liquid simulations. Our simulations indicate that ${}^1\text{Fe}(\text{CO})_4\text{-OH}$ can either coordinate via the axial or equatorial position, where we find a short (few ps) coordination in the equatorial position. In Fig. 3.10(c), the binned Kohn-Sham energies for the two $\text{Fe}(\text{CO})_4$ simulations indicate that lowest energy structures of $\text{Fe}(\text{CO})_4$ in ethanol exist in the singlet state bound to an ethanol molecule.

Based on the $g(r)$ for the $\text{Fe}-\text{O}_\text{H}$ distance, we find the Fe-O coordinate to be a key variable in connecting the two simulations. Through DFT optimization and upon inspection of the representative structures in Fig. 3.10(b), we additionally find the axial C-Fe-C angle to be an additional variable in

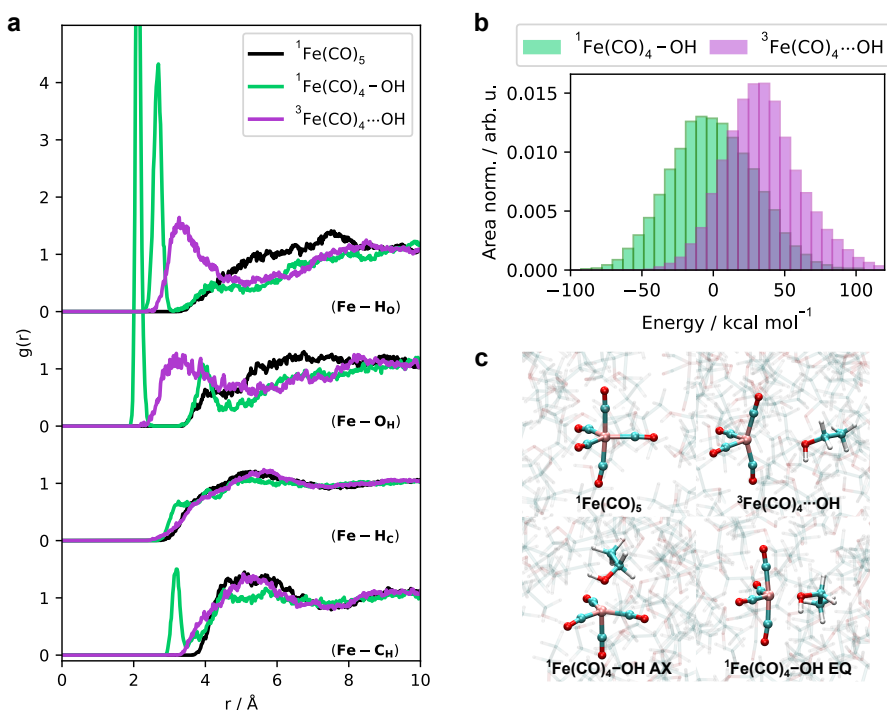


Figure 3.10: (a) Radial distribution functions $g(r)$ sampled from the $^1\text{Fe(CO)}_5$, $^1\text{Fe(CO)}_4\text{-OH}$ and $^3\text{Fe(CO)}_4$ simulations. The coordination around the iron complexes are seen in $g(r)$ for Fe-HO, Fe-OH, Fe-HC and Fe-CH. Results for $^1\text{Fe(CO)}_5$ are coloured black, for $^1\text{Fe(CO)}_4\text{-OH}$ are coloured green and for $^3\text{Fe(CO)}_4$ are coloured pink. (b) The distribution of the potential energies from the $^1\text{Fe(CO)}_4\text{-OH}$ and $^3\text{Fe(CO)}_4$ simulations, following the same colour scheme. Both energy distributions are area normalized and the mean of the singlet trajectory is used as reference energy. (c) Representative snapshots from each AIMD simulations, from which two distinct configurations are observed in the $^1\text{Fe(CO)}_4\text{-OH}$ simulation. Figure and caption adapted from **Paper III**.

connecting the two simulations. In Fig. 3.11, we plot the C-Fe-C angles for the two simulations to show that in addition to the Fe-O distance, there is indeed a second well defined variable.

The analysis of our simulations address the main structural features that would govern the ISC between the singlet and triplet states of Fe(CO)_4 . In the forthcoming section, our experimental data suggests a depletion of the triplet state on the order of ≈ 50 ps, concurrent with the rise in the singlet state. In this study, however, we lack the computational tools to determine the rate of ISC or the true mechanistic pathway.

The hydroxyl (-OH) and alkyl (-CH) bonds in ethanol permit the possibility

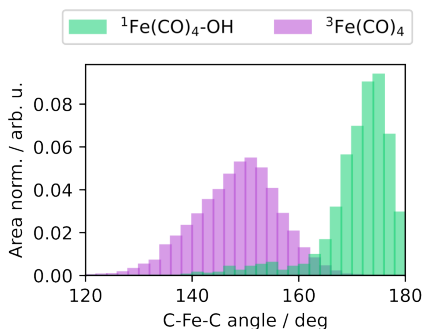


Figure 3.11: The C-Fe-C axial angles in from the $^1\text{Fe(CO)}_4$ and $^3\text{Fe(CO)}_4$ AIMD simulations. Adapted from Fig. 5(a) in **Paper III**

of two coordination sites with Fe(CO)_4 . In the forthcoming section, our experimental data and associated theoretical simulations suggest the possibility of a transiently populated alkyl coordination with Fe(CO)_4 that interconverts to the hydroxyl coordination described in Fig. 3.10. We explored this type of coordination by restraining coordination to the alkyl sites of the ethanol, followed by a release and unsupervised equilibration. The results of this type of coordination are presented in Fig. 3.12.

Here we show an explicit comparison between the hydroxyl coordination to highlight the differences. Our results can answer a question of *if there a preferential association of one type of bonding?* We find that both types of bonding are possible (confirming the experimental hypothesis in the forthcoming experimental section), however, as indicated by the experimental results, the alkyl coordination is likely formed transiently en route to the hydroxyl coordination. This is evidenced by the shifts in the Kohn-Sham energy distributions in Fig. 3.12(b), where the hydroxyl coordination (green) is the more stable species in the singlet state when compared to the corresponding alkyl coordination (red/orange). We attribute this transient coordination to the inherent weakness of the alkyl coordination relative to the hydroxyl coordination. As shown in Fig. 3.12(c), the coordination of the C-H group occurs via the bonding σ -molecular orbital, rather than from a lone pair of electrons. This type of bonding occurs with a non-linear Fe-H-C angle that reduces the overlap between the molecular orbitals on each fragment.

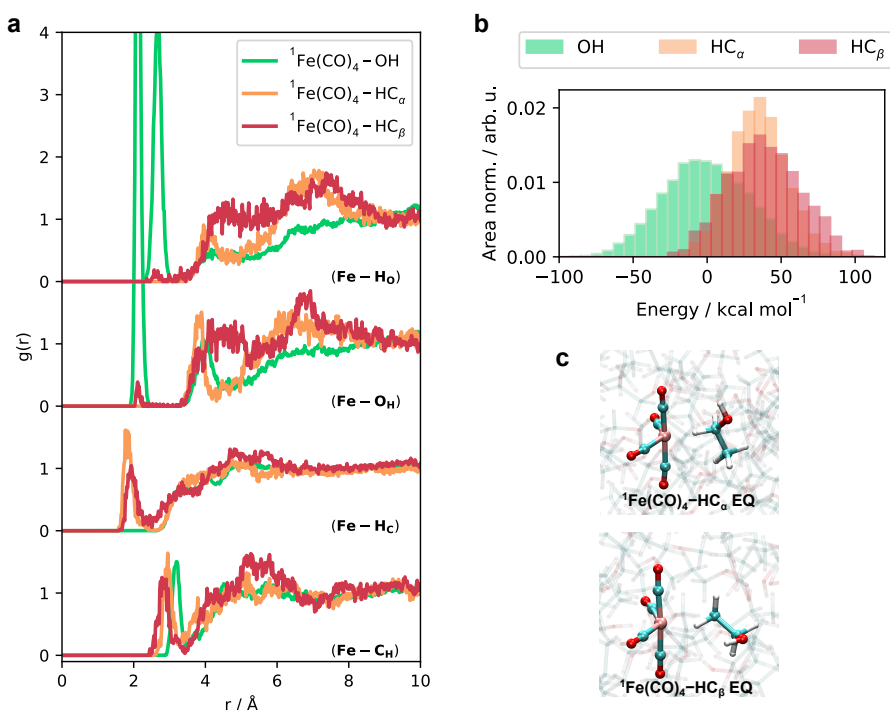


Figure 3.12: (a) Radial distribution functions $g(r)$ sampled from the $^1\text{Fe}(\text{CO})_4\text{-OH}$ (reproduced from Fig. 3.10), $^1\text{Fe}(\text{CO})_4\text{-HC}_\alpha$ and $^1\text{Fe}(\text{CO})_4\text{-HC}_\beta$ simulations. The coordination around the iron complexes are seen in $g(r)$ for Fe-H_O, Fe-O_H, Fe-H_C and Fe-C_H. The distances from $^1\text{Fe}(\text{CO})_4\text{-OH}$ are coloured green, from $^1\text{Fe}(\text{CO})_4\text{-HC}_\alpha$ are coloured orange and from $^1\text{Fe}(\text{CO})_4\text{-HC}_\beta$ are coloured red. (b) The distribution of the potential energies from the $^1\text{Fe}(\text{CO})_4\text{-OH}$ (reproduced from Fig. 3.10), $^1\text{Fe}(\text{CO})_4\text{-HC}_\alpha$ and $^1\text{Fe}(\text{CO})_4\text{-HC}_\beta$ simulations, following the same colour scheme. All energy distributions are area normalized to account for the differences in simulation length. (c) Representative snapshots from the AIMD simulations for the two distinct minima observed between the Fe-CH coordinated simulations. Figure and caption adapted from **Paper III**.

3.2.2 Probing transient species following photodissociation of $\text{Fe}(\text{CO})_5$ by picosecond L-edge spectroscopy

In **Paper III** we found that there existed many distinct structures of $\text{Fe}(\text{CO})_4$ in the singlet state and in particular, the large difference in bonding types between the singlet and triplet states. This provides a suitable foundation for experimental comparison. In the following section, the long time dynamics are probed by Fe L-edge X-ray absorption spectroscopy. The measurements were performed at the UE52-SGM beamline at the BESSY II storage ring (HZB, Berlin) [26] where the photoinduced dynamics of $\text{Fe}(\text{CO})_5$ were initiated by 258 nm pump pulse and subsequently probed by Fe $2p \rightarrow 3d$ L-edge X-ray absorption spectroscopy. These results are summarized in Fig. 3.13.

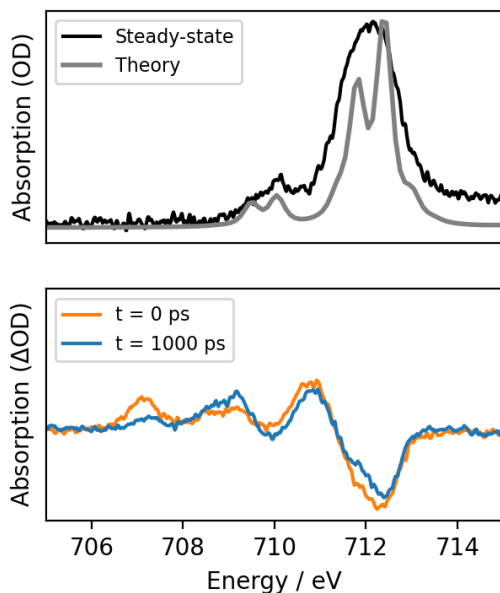


Figure 3.13: Top: Unpumped Fe 3d L-edge XAS spectrum (denoted “steady-state”) shown in black and the RAS(14,1,2;3,4,7)/TZVP simulated spectrum for $\text{Fe}(\text{CO})_5$ optimized in D_{3h} symmetry. Bottom: The two transient spectra at $t = 0$ ps (orange) and $t = 1000$ ps (blue) following excitation by a 258 nm femtosecond pump pulse. These correspond to the differences between the pumped and unpumped spectra.

The Fe 3d L-edge XAS spectrum corresponding to the “unpumped” $\text{Fe}(\text{CO})_5$ shows a pre-edge feature centered at 710.5 eV and a main edge feature centered at 712.5 eV. To assess this, Fe L-edge XAS spectra were simulated by a RASSCF wavefunction. The active space was constructed by plac-

ing the three 2p orbitals in RAS1 allowing for at most 1 hole, four occupied orbitals in RAS2 and seven unoccupied orbitals in RAS3 allowing at most 2 particles into the subspace. The resulting wavefunction is denoted RAS(14,1,2;3,4,7). The analysis of simulated RASSCF spectra assign the pre-edge feature to a $2p \rightarrow 3d_{z^2}$ “LUMO” transition and the main edge to a $2p \rightarrow e'^*$ (see Fig. 3.2 in Sec. 3.1.1) and to higher energy π_{CO}^* orbitals.

The release of CO by the pump laser pulse results in the dynamics of $\text{Fe}(\text{CO})_4$ in the singlet and triplet ground states. The bottom panel of Fig. 3.13 shows two transient spectra recorded at $t = 0$ ps and $t = 1000$ ps, where the $t = 0$ ps is recorded for a time at 45 ps within the time-resolution of the probe pulse width (90 ps). We find the depletion of the steady-state spectrum and a shifting of the pre-edge to lower energies. This produces a small region containing two peaks at 709.5 eV and 708.5 eV and a distinctly separated peak at 707 eV. At the long time delay, the first peak at 709.5 eV increases, the second peak at 708.5 eV remains in place and the low energy peak at 707 eV decreases. We explore the identity of the peaks based on the indications from the AIMD simulations in the previous section. To do this we simulate the Fe 3d L-edge XAS spectrum for the $^3\text{Fe}(\text{CO})_4$ (green) $^1\text{Fe}(\text{CO})_4$ -CH EQ (blue) and $^1\text{Fe}(\text{CO})_4$ -OH AX (red) species in Fig. 3.14.

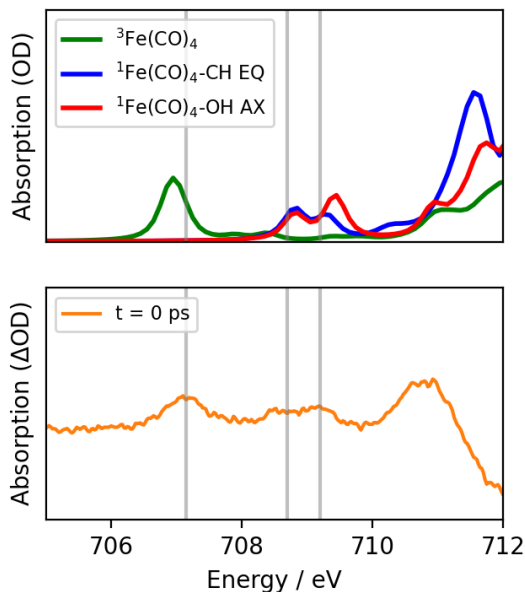


Figure 3.14: Top: the RAS(14,1,2;3,4,7)/TZVP simulated spectrum for $^3\text{Fe}(\text{CO})_4$ (green) $^1\text{Fe}(\text{CO})_4$ -CH EQ (blue) and $^1\text{Fe}(\text{CO})_4$ -OH AX (red) optimized in C_1 symmetry. Bottom: The transient spectra at $t = 0$ ps (orange).

Our simulated spectra indicate that the main species identified in the AIMD simulations map well onto the measured spectra. All spectra are given a baseline energy shift corresponding to the alignment of the $\text{Fe}(\text{CO})_5$ simulated spectrum to the steady state spectrum in Fig. 3.13. In Fig. 3.15 we display the transient spectra for $t = 1000$ ps.

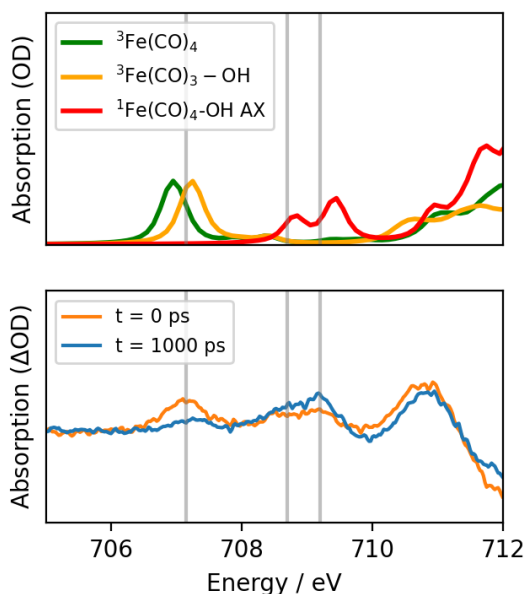


Figure 3.15: Top: the RAS(14,1,2;3,4,7)/TZVP simulated spectrum for $^3\text{Fe}(\text{CO})_4$ (green) $^3\text{Fe}(\text{CO})_3\text{-OH}$ (orange) and $^1\text{Fe}(\text{CO})_4\text{-OH AX}$ (red) optimized in C_1 symmetry. Bottom: The transient spectra at $t = 0$ ps (orange) and $t = 1000$ ps (blue).

In the previous section we found that the $^1\text{Fe}(\text{CO})_4\text{-OH AX}$ configuration was the most stable species between the possible coordination types of $^1\text{Fe}(\text{CO})_4$. By 1000 ps we therefore expect this species to be the dominant complex in solution. Our simulated spectra corroborate this view, as the spectral features at 709.5 eV increase. In addition we find that the triplet peak “persists” but that the position shifts to higher energy. In light of the reaction scheme in Fig. 1.2, we expect that by 1000 ps, that the triplet would have ISC to the singlet state within at least 100 ps. Instead we propose based on previous data, [45] that $^3\text{Fe}(\text{CO})_4$ loses an addition CO through a thermal process to coordinate the ethanol via the hydroxyl group. This yields a new transient complex not found in the AIMD simulations which corresponds to $^3\text{Fe}(\text{CO})_3\text{-OH}$, coordinating an ethanol via the hydroxyl group.

Our results are preliminary and in the next section we explore a more com-

plete analysis of the Cr 3d L-edge X-ray absorption spectroscopy which employs the same tools used in this section. Nevertheless we find a utility in identifying transient reactive metal complexes from quantum chemistry optimization and molecular dynamics simulation so that we can simulate their spectral signatures. Our work builds on a library of experimental studies, however, there is a particular value in allowing theoretical simulation to predict and identify the transient species that are needed to disentangle experimental spectra.

3.2.3 Probing transient species of photodissociated $\text{Cr}(\text{CO})_6$ by picosecond L-edge spectroscopy

The photoinduced dynamics of $\text{Cr}(\text{CO})_6$ in solution follow a similar mechanistic pathway to $\text{Fe}(\text{CO})_5$ as shown in Fig. 3.16.

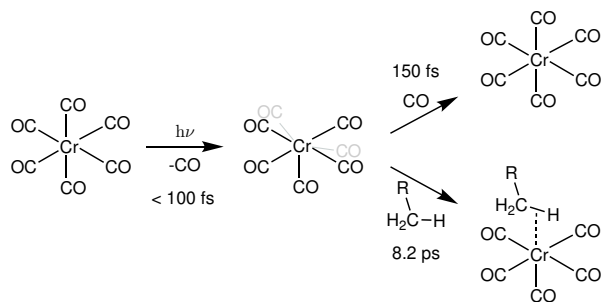


Figure 3.16: The photochemical pathways of $\text{Cr}(\text{CO})_6$ following the photoinduced release of CO. Reproduced from Scheme 3 in **Paper IV**.

In alkane solution, the vibrationally hot photoproduct $\text{Cr}(\text{CO})_5$ persists in the liquid until it coordinates an alkane molecule via the alkane ($-\text{HC}$) bond. Like the alkyl coordination in $\text{Fe}(\text{CO})_4$, this is a three center, two electron bond that forms between the C-H σ -bond and an unoccupied chromium 3d orbital. In competition with alkyl coordination is a possibility of geminate recombination, [2] whereby the released CO re-coordinates the photoproduct $\text{Cr}(\text{CO})_5$ to yield the starting molecule $\text{Cr}(\text{CO})_6$. This is exclusively an effect of the solvation, where in the gas-phase release of CO from $\text{Cr}(\text{CO})_6$, we do not find evidence of recombination.

The photoinduced CO release from $\text{Cr}(\text{CO})_6$ was initiated by a 259 nm pump laser and subsequently probed by Cr 2p \rightarrow 3d L-edge X-ray absorption spectroscopy (in range 570 - 595 eV). The spectra corresponding to “unpumped” $\text{Cr}(\text{CO})_6$ are shown in Fig. 3.17(a). In addition, the O 1s \rightarrow π^* K-edge spectra were measured in the range 520 - 540 eV. The corresponding spectra of the unpumped $\text{Cr}(\text{CO})_6$ are shown in Fig. 3.17(b).

The Cr L-edge XAS spectra were simulated by a RASSCF wavefunction which placed the three 2p orbitals in RAS1 allowing for at most 1 hole, five occupied orbitals in RAS2 and 11 unoccupied orbitals in RAS3 allowing at most 2 particles into the subspace. The resulting wavefunction is denoted RAS(16,1,2;3,5,11). This wavefunction resulted in a good agreement with the experimental spectrum and provided a basis to study the reaction coordinate.

Two time-resolved spectra were obtained for both the Cr L-edge and the O K-edge, though we will only detail the findings in relation to the L-edge here. The time-resolved spectra recorded at a time delay of 90 ps and 50 ns

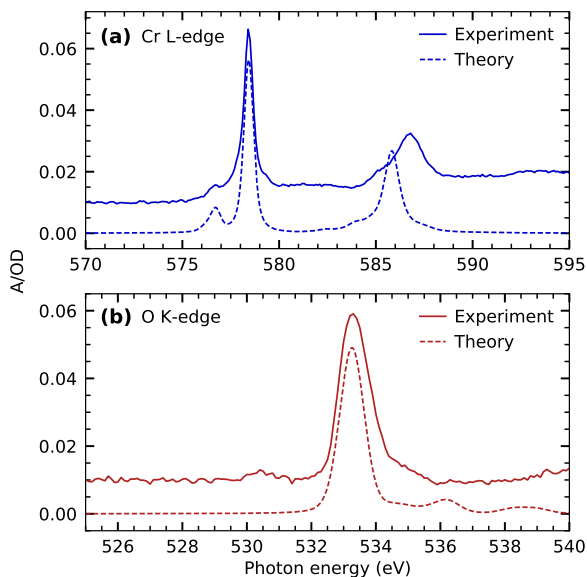


Figure 3.17: Steady-state X-ray absorption spectra of $\text{Cr}(\text{CO})_6$ in octane solution measured at the (a) Cr L-edge and (b) O K-edge compared with calculated spectra at the RASSCF and TD-DFT level of theory, respectively. Figure and caption adapted from Fig. 4 in **Paper IV**.

as shown in Fig. 3.18 and show essentially the same spectral features. The ground state spectral features are depleted and there is a pre-edge feature shifted to lower energy at 574.9 eV.

In addition to the RASSCF calculations of $\text{Cr}(\text{CO})_6$ we optimized $\text{Cr}(\text{CO})_5$ and $\text{Cr}(\text{CO})_5$ -butane so that we could simulate their XAS spectra. Butane was chosen instead of octane to reduce the computational cost. The same RASSCF active space was optimized for the two additional complexes and we show the $\text{Cr}(\text{CO})_5$ spectrum in red and the $\text{Cr}(\text{CO})_5$ -butane spectrum in blue. We find that like the Fe L-edge XAS in Sec. 3.2.2 show a spectral dependence on the coordination of the metal complex, the same holds true for the complexation of $\text{Cr}(\text{CO})_6$. The simulated spectra show that lowest energy feature of $\text{Cr}(\text{CO})_6$ shifts down in energy for $\text{Cr}(\text{CO})_5$ and then shifts back up in energy following coordination of a solvent molecule to form $\text{Cr}(\text{CO})_5$ -butane. We note here that the shift down in energy is larger than the shift up in energy, which is largely attributed to the strength of the bond which forms between $\text{Cr}(\text{CO})_5$ and a ligand (CO vs. butane).

By disentangling our RASSCF results, we find that the reason for the shifting pre-edge feature is due to the shifts in orbital energies. The LUMO of $\text{Cr}(\text{CO})_5$ shifts down in energy after the octahedral symmetry of $\text{Cr}(\text{CO})_6$ is broken. This LUMO is increased in energy following a stabilization of the

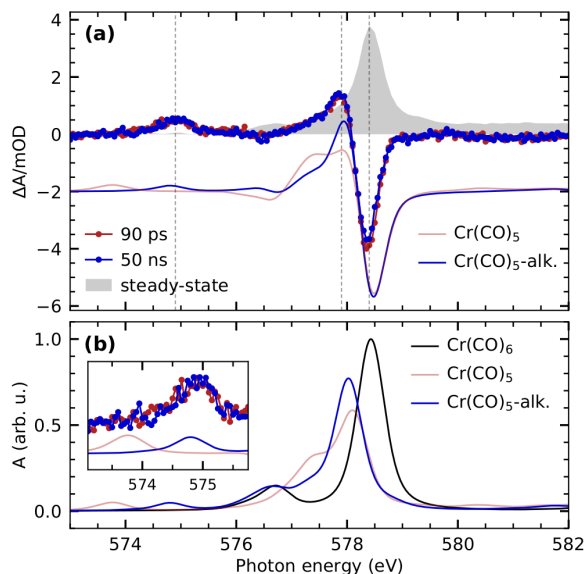


Figure 3.18: Experimental and calculated transient Cr L-edge X-ray absorption difference spectra of Cr(CO)_6 in octane solution. Figure partially reproduced from Fig. 5 in **Paper IV**.

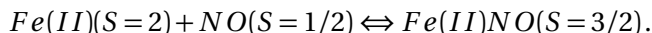
bonding molecular orbital pair when the metal-alkane σ -bond is formed. While the free Cr(CO)_5 is not observed experimentally, in **Paper IV**, the vibrationally hot Cr(CO)_5 is observed in the transient absorption spectra within the first picosecond. We anticipate that these shifts in orbital energies and hence the shifts in spectral features of the L-edge spectra would be revealed with femtosecond resolution.

3.3 From CO to NO

In a larger context, carbonyl dissociation from a metal complex is often grouped into a class of carbonyl containing molecules called photoinduced CO releasing molecules (PhotoCORMs). [57; 72] These have novel application in biological systems, where visible light induces a release of CO into the cells in a targeted release. In doing so the CO is liberated and the remaining metal complex can bind with an available solvent in the medium. Another closely related class of molecules replaces the CO with a nitrosyl (NO) ligand giving the photoinduced NO releasing molecules (PhotoNORMs). [27] In addition to carbon monoxide and hydrogen sulfide (H₂S), nitric oxides act as signalling molecules in biological systems.[18] Due to the ease of “liberating” the nitrosyl ligand from the parent metal complex, transition metal complexes containing nitrosyl ligands have use in triggered reactions with the surrounding solvent. A complication of metal nitrosyls is a particular “non-innocence” of the ligand which arises from the placement of the valence electrons in the metal d-orbitals and the nitrosyl π^* orbitals. The electronic structures of these nitrosyl containing molecules are often complicated and require a multiconfigurational treatment. To study this class of molecules, we considered the simplest aqueous iron nitrosyl complex, the “brown-ring” complex or $[\text{Fe}(\text{H}_2\text{O})_5(\text{NO})]^{2+}$.

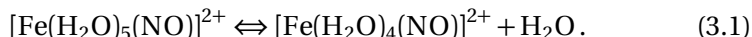
3.3.1 Dynamics and electronic structure of an aqueous nitrosyl

The “brown-ring” reaction is a standard undergraduate test in a chemistry lab to determine the presence of nitrates in aqueous solution. Experimentally, the the addition of an aqueous solution of an Fe(II) precursor complex to a solution that contains nitric oxide results in a brown layer at the liquid-liquid interface: [40–42]



The complex formed in the brown layer between the liquid-liquid interface is referred to as the “brown-ring” complex. The complex that is formed weakly binds the nitrosyl, whereby heating or shaking the solution results in the dissipation of the brown layer. For this reason, the isolated “brown-ring” complex was not isolated until 2019, when Monsch and Klüfers obtained a crystal structure of the salt of the “brown-ring” complex. [44] This prompted us to simulate the “brown-ring” complex in its quartet ground state to investigate the structure and dynamics of the complex in aqueous solvent. In **Paper V** we performed liquid AIMD simulations using the CPMD algorithm at 300 K in the NVT ensemble along with the BP86 pure DFT functional. We found that there exists a dynamical equilibrium formed

between the conventional pseudo-octahedral “brown-ring” complex and a square pyramidal structure upon loss of a coordinating water ligand:



This process is summarized Fig. 3.19, where we found three distinct types of structures: the conventionally established “brown-ring” complex in a pseudo-octahedral structure in Fig. 3.19(a), the dissociated pseudo-octahedral structure in Fig. 3.19(b) and the square-pyramidal structure in Fig. 3.19(c) that forms a hydrogen bond with the former water ligand.

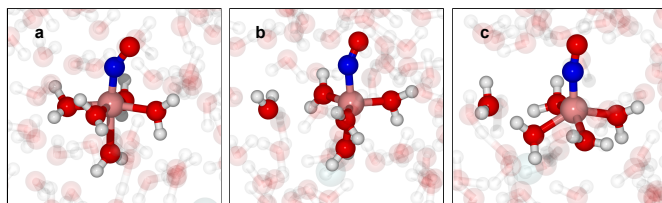


Figure 3.19: Snapshots taken from the simulation showing the equilibrium between $[\text{Fe}(\text{H}_2\text{O})_5(\text{NO})]^{2+}$ and $[\text{Fe}(\text{H}_2\text{O})_4(\text{NO})]^{2+}$ through the exchange of one H_2O . (a) shows the octahedral $[\text{Fe}(\text{H}_2\text{O})_5(\text{NO})]^{2+}$ complex. (b) The intermediate state with one equatorial H_2O molecule dissociating from the penta-aqua complex. (c) depicts the formation of the square-pyramidal $[\text{Fe}(\text{H}_2\text{O})_4(\text{NO})]^{2+}$ complex, Figure and caption adapted from Fig. 1 in **Paper V**.

In order to quantify this equilibrium, we constructed RDFs corresponding to the five shortest $\text{Fe}-\text{O}_\text{W}$ distances. We did this in order to see how the water ligands solvate the metal center throughout the simulation. In Fig. 3.20, we show the individually normalized $g(r)$ corresponding to the five closest water molecules. We found that the fifth water shows a broad distribution at short distances, indicating that the bond is more “loose” than the other water ligands and that there is a clear bimodal distribution indicating the presence of the tetra-aqua coordinated “brown-ring” complex.

We showed in **Paper V** that while there exists no large energetic difference between the two structures (> 10 kcal/mol), there was a pronounced effect on the UV spectrum in relation to the subtle shifts of the occupied and unoccupied orbitals between the two structures (see **Paper V**).

We were acutely aware of the mutlireference character of many iron nitrosyl complexes and in particular with the “brown-ring” complex. This knowledge builds on work by Radon *et al.* [54] and Monsch and Klüfers, [44] where in the former, the authors provided benchmark CASSCF results detailing contributing electron configurations in the composition of the quar-

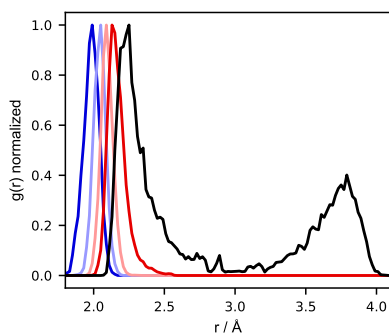


Figure 3.20: Radial distribution functions, $g(r)$, renormalized at the first peak to enhance features, for the five coordinating water molecules with respect to the Fe center for the Fe-O_W distance. Figure and caption adapted from Fig. 1 in **Paper V**.

tet and doublet ground states. To address the muticonfigurational character ourselves, we optimized the CASSCF wavefunction corresponding to an active space shown in Fig. 3.21.

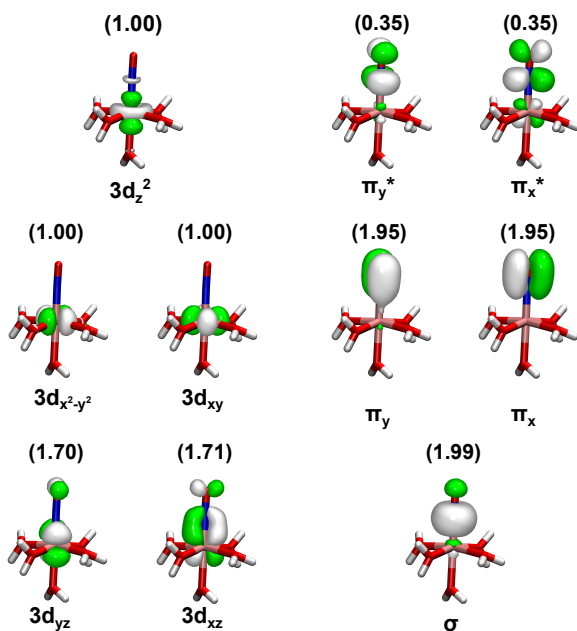


Figure 3.21: Molecular orbital diagram corresponding to the CAS(13e,10o) active space used in the NEVPT2 calculations. The natural orbital occupations corresponding to the SA(1Q+1S)-CAS(13e,10o)/NEVPT2 + CPCM(water) calculation are displayed above in parentheses. Figure and caption reproduced from **Paper VI**.

The classically established octahedral structure was optimized at the TPSSh/def2-TZVP + CPCM(water) level of theory and then an active space was selected for the CASSCF calculation that contained the iron 3d orbitals and the relevant bonding and antibonding nitrosyl σ , π and π^* orbitals. This level of theory is formally denoted CAS(13e,10o)/def2-TZVP + CPCM(water) and hereafter we simply refer to it as CAS(13e,10o). Shown in above each orbital are the natural orbital populations. We can see immediately that the non-zero occupations of the unoccupied orbitals are indicative of this “non-innocence” of the coordinating nitrosyl. This non-innocence of the nitrosyl ligand is a direct result of the multiconfigurational character in the quartet ground state. In Eq. 3.2, we display the set of electron configurations which make up the quartet ground state wavefunction.

$$\begin{aligned}
{}^4\Psi_1 \text{ (53.9 \%)} &: (\sigma)^2(\pi_y)^2(\pi_x)^2(d_{xz})^2(d_{yz})^2(d_{z^2})^\uparrow(d_{xy})^\uparrow(d_{x^2-y^2})^\uparrow(\pi_y^*)^0(\pi_x^*)^0 \\
{}^4\Psi_2 \text{ (13.6 \%)} &: (\sigma)^2(\pi_y)^2(\pi_x)^2(d_{xz})^2(d_{yz})^\uparrow(d_{z^2})^\uparrow(d_{xy})^\uparrow(d_{x^2-y^2})^\uparrow(\pi_y^*)^\downarrow(\pi_x^*)^0 \\
{}^4\Psi_3 \text{ (12.5 \%)} &: (\sigma)^2(\pi_y)^2(\pi_x)^2(d_{xz})^\uparrow(d_{yz})^2(d_{z^2})^\uparrow(d_{xy})^\uparrow(d_{x^2-y^2})^\uparrow(\pi_y^*)^0(\pi_x^*)^\downarrow \\
{}^4\Psi_4 \text{ (6.5 \%)} &: (\sigma)^2(\pi_y)^2(\pi_x)^2(d_{xz})^\uparrow(d_{yz})^\uparrow(d_{z^2})^\uparrow(d_{xy})^\uparrow(d_{x^2-y^2})^\uparrow(\pi_y^*)^\downarrow(\pi_x^*)^\downarrow \\
{}^4\Psi_5 \text{ (5.3 \%)} &: (\sigma)^2(\pi_y)^2(\pi_x)^2(d_{xz})^2(d_{yz})^0(d_{z^2})^\uparrow(d_{xy})^\uparrow(d_{x^2-y^2})^\uparrow(\pi_y^*)^2(\pi_x^*)^0
\end{aligned} \tag{3.2}$$

We found that the electron configuration which would place all electrons within the Fe 3d orbitals (${}^4\Psi_1$) only accounts for 53.9% of the ground state wavefunction, meaning that the nitrosyl plays an active role in determining the composition of the ground state wavefunction. By contrast, we found the sextet ground state to be predominantly described by a single electron configuration, ${}^6\Psi_1$ which involved

$$\begin{aligned}
{}^6\Psi_1 \text{ (88.5 \%)} &: (\sigma)^2(\pi_y)^2(\pi_x)^2(d_{xz})^2(d_{yz})^\uparrow(d_{z^2})^\uparrow(d_{xy})^\uparrow(d_{x^2-y^2})^\uparrow(\pi_y^*)^\uparrow(\pi_x^*)^0 \\
{}^6\Psi_2 \text{ (2.9 \%)} &: (\sigma)^2(\pi_y)^2(\pi_x)^2(d_{xz})^\uparrow(d_{yz})^2(d_{z^2})^\uparrow(d_{xy})^\uparrow(d_{x^2-y^2})^\uparrow(\pi_y^*)^0(\pi_x^*)^\uparrow
\end{aligned} \tag{3.3}$$

In an effort to understand the fluctuations in the multiconfigurational character in both spin states, we reproduced the results of the quartet simulation in **Paper VI** and repeated the AIMD simulations in sextet ground state. We found that the main structural differences between the two simulations were in the description of the Fe-N distance, where on average, the quartet displayed a shorter Fe-N distance. Based on these structural differences,

we were motivated to probe the Fe-N distance coordinate in order to connect the two spin states. To do this, we return to an “isolated system” based on the TPSSh/def2-TZVP + CPCM(water) optimized structure. A rigid scan was constructed over the Fe-N distance corresponding to 1.62–3.27 Å, by taking the optimized structure and performing displacements. Based on these rigid scan geometries we determined the CAS(13e,10o) wavefunction in the quartet and sextet ground states simultaneously. In this state-averaged CASSCF calculation, denoted SA(1Q+1S)-CAS(13e,10o), we additionally performed a NEVPT2 calculation on the CASSCF reference states. The results of this rigid scan are shown in Fig. 3.22(a).

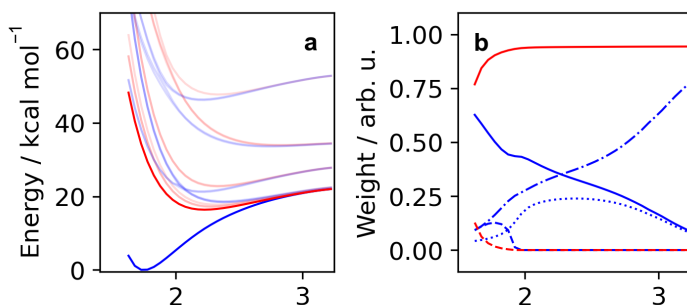


Figure 3.22: State properties for a rigid scan along the Fe-N scan calculated for the quartet (blue) and sextet (red) states at the SA(10Q+9S)-CAS(13e,10o)/NEVPT2 level of theory. (a) Potential energy curves of the electronic states. The ground state quartet and sextet states are shown bolded, with all excited states shown more transparent. (b) Weights of leading quartet electron configurations ${}^4\Psi_1$ (solid blue), ${}^4\Psi_2$ (dot-dashed blue), ${}^4\Psi_3$ (dashed blue) and ${}^4\Psi_5$ (dotted blue) and the leading sextet electron configurations ${}^6\Psi_1$ (solid red) and ${}^6\Psi_2$ (dashed red). Figure and caption partially adapted from **Paper VI**.

It is immediately clear that the quartet (blue) and sextet (red) ground states are connected by the Fe-N distance. In Fig. 3.22(a) we additionally calculate 9 quartet and 8 sextet excited states (shown semi-transparent) to highlight the possibility of state degeneracies. Based on the CASSCF wavefunction, we extracted the electron configurations corresponding to Eq. 3.2 and Eq. 3.3 from the quartet and sextet ground states, respectively. The results of this scan are shown in Fig. 3.22(b). The quartet weights displayed correspond to ${}^4\Psi_1$ (solid blue), ${}^4\Psi_2$ (dot-dashed blue), ${}^4\Psi_3$ (dashed blue) and ${}^4\Psi_5$ (dotted blue). The sextet weights displayed correspond to ${}^6\Psi_1$ (solid red) and ${}^6\Psi_2$ (dashed red). We find a few important points upon analysis of this scan. The sextet state is *essentially* described by a single electron configuration, with a small deviation at very short distances. The quartet state becomes even more multiconfigurational as the Fe-N bond is elon-

gated until it becomes dominated by a single electron configuration at the end of the scan.

We re-connect the rigid Fe-N scan to the AIMD simulations by means of a structural sampling. The sampling scheme consisted of 100 randomly sampled geometries from each of the quartet and sextet simulations. Within the 100 points sampled, 50 corresponded to the pseudo-octahedral “brown-ring” complex and 50 corresponded to the hydrogen bonded square-pyramidal complex defined in Eq. 3.1. We display the results of this sampling in Fig. 3.23, where the pseudo-octahedral “brown-ring” configurations are coloured red and the square-pyramidal “brown-ring” configurations are coloured blue. Additionally the points sampled from the quartet simulation are bold while those from the sextet simulation are hollow.

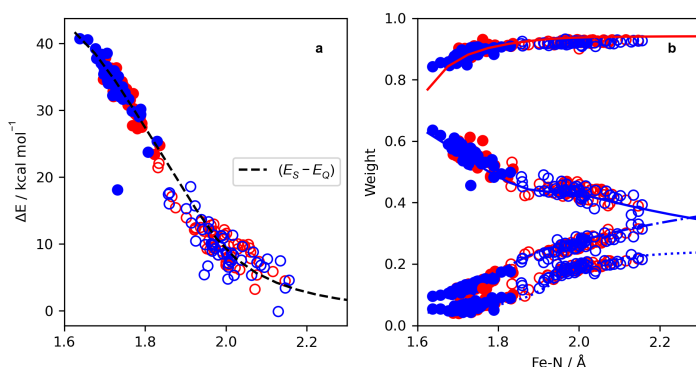


Figure 3.23: Difference in NEVPT2 energies (sextet–quartet) for geometries sampled from the quartet and sextet trajectories. The penta-aqua sampled geometries are shown in red and the tetra-aqua sampled geometries are shown in blue. The geometries sampled from the quartet trajectory are shown as solid, while the geometries sampled from the sextet trajectory are shown to be hollow. The difference in energy taken from the model potentials in Figure 5a is shown by the dashed black line. Figure and caption reproduced from **Paper VI**.

In Fig. 3.23(a) we re-express the quartet and sextet ground state energies as a difference energy (dashed line) so that the geometric distortions induced by the bulk liquid can be subtracted off from each state. Following this, the sampled geometries show a distinct correlation with the rigid Fe-N scan energies. We similarly find an excellent agreement with the sampled electron configuration weights in Fig. 3.23(b). Using this data, we examined other possible correlations, Fe-N-O angle, N-O distance, Fe-O_W etc. with the electronic properties but found no similar agreement. One takeaway is that the penta-aqua and tetra-aqua complexes do not change the electronic structure significantly and instead the large changes in electronic

structure are contained within the FeNO moiety.

To summarize, we find a particular utility in doing AIMD simulations such that mechanistic information (**Paper V**) and structural comparisons (**Paper VI**) can be elucidated. Our supporting quantum chemistry calculations and structural sampling enabled the study of a multiconfigurational wavefunction encoded within the liquid dynamics.

4. Conclusion and outlook

In this thesis, we have studied some fundamental ingredients in homogeneous catalytic reactions. We have done this so that we can learn about the changes in electron configuration, in spin states, in coordination, and in solvation that result when a metal complex begins a catalytic reaction. These changes are largely related to the initial steps in the reaction which cause a metal complex to become undercoordinated, resulting in a reactive metal center. Through a combination of quantum chemistry calculations and molecular dynamics simulations, we have defined a toolkit to study the dynamics of these complexes and in particular our model metal carbonyl system $\text{Fe}(\text{CO})_5$.

High-level electronic structure methods based on primarily multiconfigurational and density functional methods have allowed us to characterize the various photoproducts of $\text{Fe}(\text{CO})_5$. In **Paper I** we were able to derive the basic excited state mechanisms that showed how synchronized bond oscillations coupled to CO release are related to the positions of bound and dissociative states. This provided a mechanistic insight and reason to explore other metal carbonyls, in particular the comparison that we made to $\text{Cr}(\text{CO})_6$ in **Paper II**. By learning the mechanisms of the initial decay, we can see how CO is released from a metal center, which is important in creating the undercoordinated metal complexes in a catalytic reaction. We can use these insights to understand how undercoordinated metal complexes are formed from a variety of metal complexes that include carbonyls and other coordinating ligands. By extending the methods to new systems, we can explore how varying metal-ligand bonding results in different excited state lifetimes and mechanistic details.

In the long time dynamics, we showed that molecular dynamics simulations are an invaluable tool to understand subtle changes in local bonding of a metal complex that can catalyze/participate in a reaction. Our results summarized in **Paper III** were able to characterize the role of coordination in the singlet state and the potential solvent mechanisms that lead to the depletion of the triplet state. These changes in multiplicity and associated differences in solute-solvent interactions are essential ingredients in a catalytic reactions involving transition metal complexes.

What we would like to explore in the future are methods which can simulate the intermediate fs - ps dynamics, tracking the release of the CO and the undercoordinated metal complex as it reacts with the available solvent. In **Paper IV** we find evidence through time-resolved spectroscopy, that the initial undercoordinated metal experiences a cooling that precedes the association of a solvent molecule. We want to be able to understand for how long a metal complex remains undercoordinated and when it does become coordinated, how that decays.

In the final part of the thesis, we offered a “mini-thesis” on the well studied but intricate electronic structure and dynamics of an aqueous nitrosyl complex. Our results show the importance of using both molecular dynamics simulation and quantum chemistry methods to understand how metal complexes exist in the liquid and the electronic structures encoded within. While we did not consider a triggered reaction for the nitrosyl complexes, our results suggest that this kind of analysis would be essential when performing such calculations. A natural extension of this kind of analysis would be to the iron porphyrin complex in hemoglobin which is known to coordinate NO. The toolkit presented in this thesis is well suited for this kind of system and future work could be heavily motivated by the present studies.

This thesis sits in a particularly good time for joint theoretical-experimental collaborations. While we are often motivated to simulate existing experimental probes, we have demonstrated that it is possible to predict future experimental “question marks”. The capability of probing the reaction coordinate on a timescale of its evolution and with energetic resolution is only getting better. Our recent work in **Paper A** shows that large scale facilities such as X-ray free electron lasers are capable of providing the needed resolution to match the theoretical predictions. In recent years, the computational efficiency of the methods employed in this thesis have improved such that many of the previously demanding tools can be used to dynamically model the spectra that are being measured. We would like to extend these methods to a metal complex that completes a full catalytic cycle. A natural type of system involves the rhodium complex ($\text{Tp}^*\text{Rh}(\text{CO})_2$) described in the introduction and the rhodium complex ($\text{CpRh}(\text{CO})_2$) described in **Paper A**. We want to study how the excited states produce the catalytically active intermediate complex and understand how ground state spin states, solvation and electron configurations allow for the breaking of the well studied C-H bond.

From a more personal perspective, I think the results in this thesis can serve as a platform for unravelling two additional aspects of $\text{Fe}(\text{CO})_5$. The first would be to explore the possibility of solvent exchange mechanisms

in the coordination of ethanol to $\text{Fe}(\text{CO})_4$ in the singlet state. In **Paper III** we showed that $\text{Fe}(\text{CO})_4$ can exchange solvent molecules as ligands. I am interested in this because we would be able to state whether an intermediate metal complex is capable of coordinating multiple solvent molecules in its lifetime, or if the complex which initially coordinates a solvent molecule associates only that molecule. This can be directly related to catalysis, where it is not clear whether solvent exchange mechanisms are present in all parts of a catalytic cycle. The second ambition would involve the direct simulation of intersystem crossing mechanisms of the intermediate $\text{Fe}(\text{CO})_4$. I want to understand how solvation and spin-orbit coupling direct the intersystem crossing in these systems, in particular how the solvent cage surrounding the triplet $\text{Fe}(\text{CO})_4$ facilitates the process.

Populärvetenskaplig sammanfattning

För att lära sig något definitivt om vilka omständigheterna som orsakar en kemisk reaktion, så måste reaktionskoordinaten mellan reaktanterna och reaktionsprodukten definieras unikt. Reaktanterna, produkter och eventuella intermediärer behöver karaktäriseras, deras relativa energier bestämmas, och möjliga mekanistiska reaktionsvägar dem emellan behöver undersökas. För att kunna kontrollera när reaktionen ska börja, så behöver vi hitta ett sätt att inducera reaktionen. I denna avhandling behandlas ljusinducerade kemiska reaktioner i vätskelösning som genererar kortlivade kemiska föreningar som kan reagera med omgivande lösningsmedel. En kombination av teoretiska och experimentella redskap har använts för att få precis information om bildande och sönderfall av dessa kortlivade föreningar.

Organometalliska föreningar, där övergångsmetaller koordineras av organiska ligander, kan användas för att katalysera kemiska reaktioner. De är ofta involverade i reaktionen som del av en reaktionsintermediär och återgår i sitt normal tillstånd när den katalytiska processen är över. Med en utlösande puls av ljus kan systemet förskjutas från jämvikt, då arrangemanget av koordinerande ligander ändras, vilket öppnar för olika reaktionsvägar.

I ett försök att förstå de inneboende skillnaderna i ett brett spektrum av organometalliska komplex, är det naturligt att starta med att undersöka olika elektronkonfigurationer hos metalljonen och dess omgivande ligander. Distinkta elektronstrukturer ger olika geometri i det organometalliska komplexet och kan förklara dess reaktivitet eller varför det är kemiskt inert. För att beskriva elektronstrukturen används robusta kvantkemiska beräkningar, ofta i kombination med molekylodynamiska simuleringar, där det organometalliska komplexet och dess omgivning kan följas på tidskalan av kemiska förändringar.

Avhandlingsarbetet har bland annat involverat studier av järnpentakarbonyl ($\text{Fe}(\text{CO})_5$) som varit ett modellsystem för att undersöka det reaktiva landskapet i en bred klass av karbonylkoordinerade organometalliska föreningar. De delar av avhandlingen som fokuserar på $\text{Fe}(\text{CO})_5$ är indelad i tre separata avsnitt (i) ultrasnabb (femtosekund-till-pikosekund) molykeldynamik

i elektroniskt exciterade tillstånd av $\text{Fe}(\text{CO})_5$ i gasfas, där kortlivade metallkomplex bildas, (ii) molekylodynamik i vätskelösning på längre tidsskala (pikosekund-till-nanosekund) i det elektroniska grundtillståndet, där olika reaktionsintermediärer bildas och (iii) simuleringar av experiment som möjliggör att undersöka de olika dynamiska processerna. Mot slutet av avhandlingen, dras paralleller mellan de väl undersökta karbonyl(CO)föreningarna och en bred klass av metallkomplex med en nitrosyl(NO)ligand.

Sammanfattningsvis, kan vi mot bakgrund av de teoretiska undersökningarna formulera meningsfulla frågor om dessa kemiska föreningar och dynamiska processer, och med entusiasm kan vi tillsammans med våra experimentella kollegor försöka besvara dessa frågor.

Nyckelord: kvantkemi, elektronstruktur, multikonfigurationell, täthetsfunktionsteori, molekylodynamik, molekylodynamik i exciterade tillstånd, Icke-adiabatisk dynamik, organometalliska komplex, röntgenabsorptionsspektroskopi, fotoelektron-spektroskopi, tidsupplöst spektroskopi, femtosekund, pikosekund

Acknowledgements

I first need to acknowledge my supervisor, Michael Odelius. With all the ups and downs of PhD life, you have always been able to keep me on track during the studies by being encouraging and supportive whenever I felt a bit lost. Thank you for those planned and spontaneous discussions which made all of the work in this thesis happen. I'm extremely grateful for your patience during the most stressful times here. I need to thank my co-supervisor Markus Kowalewski who showed me how to do real quantum dynamics simulations. It's been a pleasure to work with you but I am still afraid of Feynman diagrams. I need to thank Åsa Larson, who has been an excellent mentor to me during my studies. Lastly, I need to thank my readers Mark and Maria who provided a lot of invaluable feedback on this thesis.

I need to thank Diana and Peo, who provided me with a cozy stuga for the majority of my stay in Sweden. It was extremely generous of you to open your home to me (a person you had never met) and give me a real introduction to Sweden. My first semla in Viggbyholm, my first real Swedish meatball, toast skagen, våffeldagen, sill, midsommar parties and many other great Swedish things were introduced to me by you. I cannot thank you enough for the many great years that I had in Åkersberga.

I need to give a big thanks Ambar Banerjee, who always had an excellent chemical intuition that elevated a lot of the work in this thesis. Even though I am chemist myself, you always managed to remind me of things I had definitely forgotten from my previous studies. Your pragmatic approach to doing simulations and calculations really helped keep the momentum going in all of the projects.

There have been several members of the Chemical Physics division who have come and gone but I would like to give thanks to a few. Cody, you were always willing to help debug some code or show me how to do some analysis which really helped me pluck out a lot of data from my simulations. Sara (Boh!) thanks for all of the good years together in the office. Berna, it's been really nice getting to know you. For my office neighbours, Sambit, I am impressed that you have managed to tolerate me for the last 3 years. I have learned a lot about India from you and I am still making an offer for a roadtrip across the country sometime soon. Thomas, I have learned a lot

from you over the last couple of years and I appreciate all of the time you spent working with me on NO₂ in those early days of your postdoc here. I've had a great time with you outside of work, observing the chaos that is Sveavägen on a Friday night. Lorenzo, somehow, our Venn diagrams intersect on the most obscure of things and I am grateful for that. I want to thank Deependra who I got to spend a lot of time with during the period of post-pandemic warming. Our many nights out and time spent doing trivia were really enjoyable times for me during my studies. Eric, Lucas, Henrik and everyone above, I have had such an enjoyable time with every lunch break, chatting about any topic that you can imagine and of course ending it with a comedic long pause.

Jonatan, you amaze me. Maddalena, I am happy that our paths were able to cross. I have been mispronouncing your name for the last 4 years but I have it figured out now that I am leaving. Bernadette, given the history of our nations, it was natural that we would find each other in good company. Sergey, it was a joy to spend all of those years riding the bus into work together. You helped me vent my frustration about PhD life and gave me a lot of much needed advice. Anita, we've only just gotten to know each other but I am grateful for the time spent together. Mathias, you've been a wonderful friend. Patrick, I'm always happy to be part of a baking duo with you. Markus, Felix and all of the people above, thanks for all of the good times.

A large part of my studies has included an enormous experimental effort on the part of the Uppsala group. I need to thank Raphael, who has hosted me in Uppsala many times and who helped me get some hands-on experience at the beamline. It's been a great time working with you and learning about the experimental side of things. We've made a couple of good projects over the last couple of years and I really admire your ability to make a project into a paper. I also need to thank Philippe, who has driven a lot of the discussion in our Wednesday 9AM SU+UU meetings. I appreciate your willingness to learn the details of the calculations and help us interpret the data together. I owe a lot of the success of our collaboration to you and Raphael, for your willingness to have open discussions about science because, at the end of the day, that's what we are after.

Finally, I need to thank my parents Les and Lil and my cousin Stephanie who have supported me throughout all of my studies. It was a bit of a shock when I decided to move some 6000 km away but our weekly calls and updates on life have made it feel like I am home. I can't express enough gratitude and love for the support you've given me.

References

- [1] Fock matrix dynamics. *Chemical Physics Letters*, 386(4):272–278, 2004. 35
- [2] geminate recombination. 2019. URL <https://doi.org/10.1351/goldbook.G02603>. 67
- [3] K. Andersson, P.-A. Malmqvist, B. O. Roos, A. J. Sadlej, and K. Wolinski. Second-order perturbation theory with a casscf reference function. *The Journal of Physical Chemistry*, 94(14):5483–5488, 1990. 28
- [4] K. Andersson, P.-A. Malmqvist, and B. O. Roos. Second-order perturbation theory with a complete active space self-consistent field reference function. *The Journal of Chemical Physics*, 96(2):1218–1226, 01 1992. 28
- [5] P. W. Atkins and R. Friedman. *Molecular quantum mechanics*. Oxford University Press, fourth edition, 2005. 40
- [6] J. A. Bearden and A. F. Burr. Reevaluation of x-ray atomic energy levels. *Reviews of Modern Physics*, 39:125–142, 1967. 40, 41
- [7] R. G. Bergman. C-H activation. *Nature*, 446(7134):391–393, 2007. 17
- [8] M. Besora, J.-L. Carreon-Macedo, A. J. Cowan, M. W. George, J. N. Harvey, P. Portius, K. L. Ronayne, X.-Z. Sun, and M. Towrie. A combined theoretical and experimental study on the role of spin states in the chemistry of $\text{Fe}(\text{CO})_5$ photoproducts. *Journal of the American Chemical Society*, 131(10):3583–3592, 2009. 18
- [9] M. Boero and A. Oshiyama. *Car-Parrinello Molecular Dynamics*, pages 1–10. Springer Netherlands, Dordrecht, 2014. 36
- [10] C. Bressler, R. Abela, and M. Chergui. Exploiting EXAFS and XANES for time-resolved molecular structures in liquids. *Zeitschrift für Kristallographie - Crystalline Materials*, 223(4-5):307–321, 2008. 43
- [11] S. E. Bromberg, H. Yang, M. C. Asplund, T. Lian, B. K. McNamara, K. T. Kotz, J. S. Yeston, M. Wilkens, H. Frei, R. G. Bergman, and C. B. Harris. The mechanism of a C-H bond activation reaction in room-temperature alkane solution. *Science*, 278(5336):260–263, 1997. 15, 17
- [12] B. R. Brooks, R. E. Bruccoleri, B. D. Olafson, D. J. States, S. Swaminathan, and M. Karplus. CHARMM: A program for macromolecular energy, minimization, and dynamics calculations. *Journal of Computational Chemistry*, 4(2):187–217, 1983. 34, 35
- [13] R. Car and M. Parrinello. Unified approach for molecular dynamics and density-functional theory. *Physical Review Letters*, 55:2471–2474, 1985. 35
- [14] J.-L. Carreón-Macedo and J. N. Harvey. Do spin state changes matter in organometallic chemistry? a computational study. *Journal of the American Chemical Society*, 126(18):5789–5797, 2004. doi: 10.1021/ja049346q. PMID: 15125671. 17

- [15] S. Choi and J. Vaníček. How important are the residual nonadiabatic couplings for an accurate simulation of nonadiabatic quantum dynamics in a quasidiabatic representation? *The Journal of Chemical Physics*, 154(12):124119, 2021. 23
- [16] M. R. Coates. Structure, dynamics and reactivity of low-oxidation state iron complexes in solution studied by ab initio molecular dynamics simulations and advanced quantum chemistry calculations., 2022. URL <https://urn.kb.se/resolve?urn=urn%3Anbn%3Ase%3Asu%3Adiva-202461>. vii
- [17] D. A. Colby, R. G. Bergman, and J. A. Ellman. Rhodium-catalyzed c-c bond formation via heteroatom-directed c-h bond activation. *Chemical Reviews*, 110(2):624–655, 2010. 15
- [18] G. M. Cooper. *The Cell: A Molecular Approach*. Sinauer Associates 2000, second edition, 2000. ISBN 0-87893-106-6. 70
- [19] W. D. Cornell, P. Cieplak, C. I. Bayly, I. R. Gould, K. M. Merz, D. M. Ferguson, D. C. Spellmeyer, T. Fox, J. W. Caldwell, and P. A. Kollman. A second generation force field for the simulation of proteins, nucleic acids, and organic molecules. *Journal of the American Chemical Society*, 117(19):5179–5197, 1995. 34, 35
- [20] R. Crespo-Otero and M. Barbatti. Cr(CO)₆ photochemistry: Semi-classical study of UV absorption spectral intensities and dynamics of photodissociation. *The Journal of Chemical Physics*, 134(16):164305, 04 2011. 53
- [21] G. Cressey, C. M. B. Henderson, and G. van der Laan. Use of L-edge x-ray absorption spectroscopy to characterize multiple valence states of 3d transition metals; a new probe for mineralogical and geochemical research. *Physics and Chemistry of Minerals*, 20(2):111–119, Jul 1993. 42
- [22] C. David Sherrill and H. F. Schaefer. The configuration interaction method: Advances in highly correlated approaches. volume 34 of *Advances in Quantum Chemistry*, pages 143–269. Academic Press, 1999. 25
- [23] J. L. Detrich, O. M. Reinaud, A. L. Rheingold, and K. H. Theopold. Can spin state change slow organometallic reactions? *Journal of the American Chemical Society*, 117(47):11745–11748, 1995. doi: 10.1021/ja00152a015. 17
- [24] W. Domcke, D. R. Yarkony, and H. Köppel. *Conical Intersections*. World Scientific, 2004. 22
- [25] K. G. Dyall. The choice of a zeroth-order hamiltonian for second-order perturbation theory with a complete active space self-consistent-field reference function. *The Journal of Chemical Physics*, 102(12):4909–4918, 1995. 29
- [26] M. Fondell, S. Eckert, R. M. Jay, C. Weniger, W. Quevedo, J. Niskanen, B. Kennedy, F. Sorgenfrei, D. Schick, E. Giangrisostomi, R. Ovsyannikov, K. Adamczyk, N. Huse, P. Wernet, R. Mitzner, and A. Föhlisch. Time-resolved soft X-ray absorption spectroscopy in transmission mode on liquids at MHz repetition rates. *Structural Dynamics*, 4(5):054902, 08 2017. 63
- [27] P. C. Ford. Metal complex strategies for photo-uncaging the small molecule bioregulators nitric oxide and carbon monoxide. *Coordination Chemistry Reviews*, 376:548–564, 2018. ISSN 0010-8545. 70
- [28] D. Frenkel and B. Smit. Chapter 1 - introduction. In D. Frenkel and B. Smit, editors, *Understanding Molecular Simulation*, pages 1–6. Academic Press, San Diego, second edition edition, 2002. ISBN 978-0-12-267351-1. 35
- [29] W. Fuss. Where does the energy go in fs-relaxation? *Chemical Physics*, 425:96–103, 2013. ISSN 0301-0104. 18
- [30] W. Fuss, S. A. Trushin, and W. E. Schmid. Ultrafast photochemistry of metal carbonyls. *Research on Chemical Intermediates*, 27(4):447–457, 2001. 18, 53
- [31] P. Hohenberg and W. Kohn. Inhomogeneous electron gas. *Physical Review*, 136:B864–B871, 1964. 29

- [32] K. P. Jensen. Bioinorganic chemistry modeled with the TPSSh density functional. *Inorganic Chemistry*, 47(22):10357–10365, 2008. 31
- [33] S. Keller, M. Dolfi, M. Troyer, and M. Reiher. An efficient matrix product operator representation of the quantum chemical Hamiltonian. *The Journal of Chemical Physics*, 143(24):244118, 12 2015. 26
- [34] K. Kunnus, I. Josefsson, I. Rajkovic, S. Schreck, W. Quevedo, M. Beye, C. Weniger, S. Grubel, M. Scholz, D. Nordlund, W. Zhang, R. W. Hartsock, K. J. Gaffney, W. F. Schlotter, J. J. Turner, B. Kennedy, F. Hennies, F. M. F. de Groot, S. Techert, M. Odelius, P. Wernet, and A. Föhlisch. Identification of the dominant photochemical pathways and mechanistic insights to the ultrafast ligand exchange of $\text{Fe}(\text{CO})_5$ to $\text{Fe}(\text{CO})_4\text{EtOH}$. *Structural Dynamics*, 3(4):043204, 02 2016. 18
- [35] D. G. Liakos, M. Sparta, M. K. Kesharwani, J. M. L. Martin, and F. Neese. Exploring the accuracy limits of local pair natural orbital coupled-cluster theory. *Journal of Chemical Theory and Computation*, 11(4):1525–1539, 2015. 33
- [36] S. Lippard and J. Berg. *Principles of Bioinorganic Chemistry*. Principles of Bioinorganic Chemistry. University Science Books, 1994. ISBN 9780935702729. URL <https://books.google.se/books?id=zGJtXzPINAUC>. 15
- [37] J. P. Lomont, S. C. Nguyen, M. C. Zoerb, A. D. Hill, J. P. Schlegel, and C. B. Harris. Observation of a short-lived triplet precursor in $\text{CpCo}(\text{CO})$ -catalyzed alkyne cyclotrimerization. *Organometallics*, 31(9):3582–3587, 2012. doi: 10.1021/om300058y. 17
- [38] J. P. Lomont, S. C. Nguyen, and C. B. Harris. Ultrafast infrared studies of the role of spin states in organometallic reaction dynamics. *Accounts of Chemical Research*, 47(5):1634–1642, 2014. 17, 18
- [39] P.-O. Löwdin. *Correlation Problem in Many-Electron Quantum Mechanics I. Review of Different Approaches and Discussion of Some Current Ideas*, pages 207–322. John Wiley & Sons, Ltd, 1958. 24
- [40] W. Manchot. Demonstrationsversuche mit ferrostickoxyd-verbindungen. *Berichte der Deutschen Chemischen Gesellschaft*, 47(2):1614–1616, 1914. 70
- [41] W. Manchot and F. Huttner. Ueber die ferroverbindungen des stickoxydes. *Liebigs Annalen*, 372(2):153–178, 1910.
- [42] W. Manchot and K. Zechentmayer. Ueber die ferroverbindungen des stickoxydes. *Liebigs Annalen*, 350(3):368–389, 1906. 70
- [43] N. Miyaura and A. Suzuki. Palladium-catalyzed cross-coupling reactions of organoboron compounds. *Chemical Reviews*, 95(7):2457–2483, 1995. 15
- [44] G. Monsch and P. Klüfers. $[\text{Fe}(\text{H}_2\text{O})_5(\text{NO})]^{2+}$, the “brown-ring” chromophore. *Angewandte Chemie International Edition*, 58(25):8566–8571, 2019. 70, 71
- [45] S. C. Nguyen, J. P. Lomont, M. C. Zoerb, A. D. Hill, J. P. Schlegel, and C. B. Harris. Chemistry of the triplet 14-electron complex $\text{Fe}(\text{CO})_3$ in solution studied by ultrafast time-resolved IR spectroscopy. *Organometallics*, 31(10):3980–3984, 2012. 65
- [46] A. M. N. Niklasson, C. J. Tymczak, and M. Challacombe. Time-reversible born-oppenheimer molecular dynamics. *Physical Review Letters*, 97:123001, 2006. 35
- [47] D. Osman, A. Cooke, T. R. Young, E. Deery, N. J. Robinson, and M. J. Warren. The requirement for cobalt in vitamin B_{12} : A paradigm for protein metalation. *Biochimica et Biophysica Acta. Molecular Cell Research*, 1868(1):118896, 2020. 15
- [48] M. J. Paterson, P. A. Hunt, M. A. Robb, and O. Takahashi. Non-adiabatic direct dynamics study of chromium hexacarbonyl photodissociation. *The Journal of Physical Chemistry A*, 106(44):10494–10504, 2002. 53

- [49] R. Perutz, O. Torres, and A. Vlček. 8.06 - photochemistry of metal carbonyls. In J. Reedijk and K. Poeppelmeier, editors, *Comprehensive Inorganic Chemistry II*, pages 229–253. Elsevier, Amsterdam, second edition, 2013. 17
- [50] F. Plasser, M. Ruckebauer, S. Mai, M. Oppel, P. Marquetand, and L. González. Efficient and flexible computation of many-electron wave function overlaps. *Journal of Chemical Theory and Computation*, 12(3):1207–1219, 2016. 38
- [51] M. Poliakoff and E. Weitz. Shedding light on organometallic reactions: the characterization of tetracarbonyliron ($\text{Fe}(\text{CO})_4$), a prototypical reaction intermediate. *Accounts of Chemical Research*, 20(11):408–414, 1987. 18
- [52] J. A. Pople, R. Seeger, and R. Krishnan. Variational configuration interaction methods and comparison with perturbation theory. *International Journal of Quantum Chemistry*, 12(S11):149–163, 1977. 26
- [53] P. Portius, J. Yang, X.-Z. Sun, D. C. Grills, P. Matousek, A. W. Parker, M. Towrie, and M. W. George. Unraveling the photochemistry of $\text{Fe}(\text{CO})_5$ in solution: Observation of $\text{Fe}(\text{CO})_3$ and the conversion between $^3\text{Fe}(\text{CO})_4$ and $^1\text{Fe}(\text{CO})_4$ (solvent). *Journal of the American Chemical Society*, 126(34):10713–10720, 2004. 18
- [54] M. Radoń, E. Broclawik, and K. Pierloot. Electronic structure of selected FeNO^7 complexes in heme and non-heme architectures: A density functional and multireference ab initio study. *The Journal of Physical Chemistry B*, 114(3):1518–1528, 2010. 71
- [55] K. Raghavachari, G. W. Trucks, J. A. Pople, and M. Head-Gordon. A fifth-order perturbation comparison of electron correlation theories. *Chemical Physics Letters*, 157(6):479–483, 1989. 32
- [56] D. M. Roundhill. *Photochemistry of Transition Metal Carbonyl and Isocyanide Complexes*, pages 217–270. Springer US, Boston, MA, 1994. ISBN 978-1-4899-1495-8. 17
- [57] U. Schatzschneider. Photocorms: Light-triggered release of carbon monoxide from the coordination sphere of transition metal complexes for biological applications. *Inorganica Chimica Acta*, 374(1):19–23, 2011. 70
- [58] N. Schuth, S. Mebs, D. Huwald, P. Wrzolek, M. Schwalbe, A. Hemschemeier, and M. Haumann. Effective intermediate-spin iron in o_2 -transporting heme proteins. *Proceedings of the National Academy of Sciences*, 114(32):8556–8561, 2017. 15
- [59] L. Serrano-Andrés and J. J. Serrano-Pérez. *Calculation of Excited States: Molecular Photophysics and Photochemistry on Display*, pages 483–560. Springer Netherlands, Dordrecht, 2012. ix, 27
- [60] P. E. Siegbahn. A new direct ci method for large ci expansions in a small orbital space. *Chemical Physics Letters*, 109(5):417–423, 1984. 26
- [61] P. T. Snee, C. K. Payne, K. T. Kotz, H. Yang, and C. B. Harris. Triplet organometallic reactivity under ambient conditions: An ultrafast UV pump/IR probe study. *Journal of the American Chemical Society*, 123(10):2255–2264, 2001. 18
- [62] P. T. Snee, C. K. Payne, S. D. Mebane, K. T. Kotz, and C. B. Harris. Dynamics of photosubstitution reactions of $\text{Fe}(\text{CO})_5$: An ultrafast infrared study of high spin reactivity. *Journal of the American Chemical Society*, 123(28):6909–6915, 2001. 18
- [63] A. Stolow, A. E. Bragg, and D. M. Neumark. Femtosecond time-resolved photoelectron spectroscopy. *Chemical Reviews*, 104(4):1719–1758, 2004. 44
- [64] J. Stöhr. *NEXAFS Spectroscopy*. Springer, first edition, 1992. 40
- [65] D. F. Swinehart. The Beer-Lambert law. *Journal of Chemical Education*, 39(7):333, 1962. 41
- [66] S. A. Trushin, W. Fuß, K. L. Kompa, and W. E. Schmid. Femtosecond dynamics of $\text{Fe}(\text{CO})_5$ photodissociation at 267 nm studied by transient ionization. *The Journal of Physical Chemistry A*, 104(10):1997–2006, 2000. 18

- [67] J. C. Tully. Molecular dynamics with electronic transitions. *The Journal of Chemical Physics*, 93 (2):1061–1071, 1990. 37
- [68] J. J. Turner, M. W. George, M. Poliakoff, and R. N. Perutz. Photochemistry of transition metal carbonyls. *Chemical Society Reviews*, 51:5300–5329, 2022. 17
- [69] H.-J. Werner and P. J. Knowles. A second order multiconfiguration SCF procedure with optimum convergence. *The Journal of Chemical Physics*, 82(11):5053–5063, 06 1985. 26
- [70] P. Wernet. Orbital-specific Mapping of Chemical Interactions and Dynamics with Femtosecond Soft X-ray Pulses. In *X-Ray Free Electron Lasers: Applications in Materials, Chemistry and Biology*. The Royal Society of Chemistry, 08 2017. ISBN 978-1-84973-100-3. ix, 16
- [71] P. Wernet, K. Kunnus, I. Josefsson, I. Rajkovic, W. Quevedo, M. Beye, S. Schreck, S. Grübel, M. Scholz, D. Nordlund, W. Zhang, R. W. Hartsock, W. F. Schlotter, J. J. Turner, B. Kennedy, F. Hennies, F. M. F. de Groot, K. J. Gaffney, S. Techert, M. Odelius, and A. Föhlisch. Orbital-specific mapping of the ligand exchange dynamics of $\text{Fe}(\text{CO})_5$ in solution. *Nature*, 520(7545):78–81, 2015. 18
- [72] M. A. Wright and J. A. Wright. PhotoCORMs: CO release moves into the visible. *Dalton Transactions*, 45:6801–6811, 2016. 70
- [73] M. Wrighton. Photochemistry of metal carbonyls. *Chemical Reviews*, 74(4):401–430, 1974. 17
- [74] D. R. Yarkony. *Nonadiabatic Derivative Couplings*. John Wiley & Sons, Ltd, 2002. ISBN 9780470845011. 23
- [75] J. P. Zobel, J. J. Nogueira, and L. González. The IPEA dilemma in CASPT2. *Chemical Science*, 8: 1482–1499, 2017. 29